

NUMERICAL MODELS OF WIND-DRIVEN
CIRCULATION IN LAKE MELVILLE, LABRADOR

CENTRE FOR NEWFOUNDLAND STUDIES

**TOTAL OF 10 PAGES ONLY
MAY BE XEROXED**

(Without Author's Permission)

AMRITPAL SINGH BHOGAL



**NUMERICAL MODELS OF WIND DRIVEN CIRCULATION
IN LAKE MELVILLE, LABRADOR**

by



Amritpal Singh Bhogal, B. Sc (Hons)

**A Thesis submitted in partial fulfillment
of the requirements for the degree of
Master of Science**

**Department of Physics
Memorial University of Newfoundland
St. John's, Newfoundland**

December, 1984

Permission has been granted to the National Library of Canada to microfilm this thesis and to lend or sell copies of the film.

The author (copyright owner) has reserved other publication rights, and neither the thesis nor extensive extracts from it may be printed or otherwise reproduced without his/her written permission.

L'autorisation a été accordée à la Bibliothèque nationale du Canada de microfilmer cette thèse et de prêter ou de vendre des exemplaires du film.

L'auteur (titulaire du droit d'auteur) se réserve les autres droits de publication; ni la thèse ni de longs extraits de celle-ci ne doivent être imprimés ou autrement reproduits sans son autorisation écrite.

ISBN 0-315-31009-X

To my parents, for their love, care and understanding.

11

Abstract

In this work, a number of numerical models have been adapted to study the wind-driven circulation of Lake Melville. The first two models examined are the steady-state and the time-dependent homogeneous models. The results indicate that the complex bottom topography forces a complicated circulation pattern which is relatively unaffected by the value of the bottom stress coefficient although the choice of such affects the current speeds directly. For a constant wind of seven meters per second, the vertically averaged horizontal velocity is about ten centimeters per second, suggesting a surface velocity of about thirty to forty centimeters per second. The third and last model is a vertically integrated two-layer model also driven by a constant wind of seven meters per second. The results from this model indicate that baroclinic effects such as near-inertial oscillations and internal waves are important, since the internal wave phenomena associated with stratified lakes dominates their dynamics. To date, no field measurements have been carried out on Lake Melville. The simulations from the models studied, in particular the two-layer model, suggest that current measurements would be valuable for model calibrations.

Acknowledgements

I would like to thank my supervisor, Dr. Tim Keliher for his guidance and encouragement during the course of this work.

The author is also grateful to Dr. Ian Webster and Dr. Alex Hay for providing some very enlightening discussions.

The assistance of Dr. T.J. Simon in the form of literature references and computer algorithms is most gratefully acknowledged.

The author also expresses gratitude to Dr. P.P. Narayanaswami for his assistance in the word processing and printing of my thesis.

The financial assistance of the Memorial University of Newfoundland in the form of a graduate fellowship and teaching assistantships is greatly appreciated.

Last, but not least, I am indebted to my parents and my family who continually encouraged me during the whole course of my programme and served as a great inspiration in my endeavors.

Table of Contents

Dedication	(i)
Abstract	(ii)
Acknowledgements	(iii)
Contents	(iv)
List of Figures	(vii)
List of Tables	(xii)
CHAPTER 1 : INTRODUCTION	(1)
1.1. Background	(1)
1.2. Motivation for the Present Study	(5)
1.3. General Factors of Circulation	(11)
1.4. Scope of the Present Study	(14)
1.5. Results of the Work	(15)
CHAPTER 2 : THE HYDRODYNAMICAL EQUATIONS OF MOTION AND CONTINUITY	(17)
2.1. General Equations for the Barotropic Model	(17)
2.2. General Equations for the Baroclinic Model	(21)
2.3. Finite Difference Forms of Derivatives	(23)
CHAPTER 3 : THE STEADY-STATE MODEL OF LAKE MELVILLE	(25)
3.1. Derivation of the Stream Function Equation	(25)

3.2.	Method of Solution	(27)
3.3.	The Input Data	(30)
3.4.	The Results of the Model	(32)
CHAPTER 4 : THE TIME-DEPENDENT BAROTROPIC MODEL OF LAKE		
MELVILLE		(39)
4.1.	Introduction	(39)
4.2.	Total Circulation Energy for Homogeneous Basins	(39)
4.3.	The Method of Solution	(40)
4.3.1.	The Staggered Grid	(40)
4.3.2.	The Boundary and Initial Conditions	(42)
4.3.3.	Numerical Solution of the Equations	(42)
4.3.4.	Prediction of the Surface Elevation	(43)
4.3.5.	Prediction of the Mass Transport Components	(43)
4.4.	Results of the Time-Dependent Model	(45)
4.4.1.	Response of Lake Melville to Wind Forcing	(45)
4.4.2.	Response of Lake Melville After Wind Cut-off	(49)
4.5.	Energy Considerations	(62)
CHAPTER 5 : THE TIME-DEPENDENT TWO-LAYER MODEL OF LAKE		
MELVILLE		(67)
5.1.	Introduction	(68)
5.2.	Total Circulation Energy for Two-Layer Basins	(68)
5.3.	The Surface and Internal Modes of a Two-Layer System	(69)
5.4.	Method of Solution	(73)
5.4.1.	The Numerical System	(73)

5.4.2. Continuity Equations	(76)
5.4.3. Momentum Equations	(77)
5.4.4. Summary of the Computer Algorithm	(78)
5.5. Results of the Model	(83)
5.5.1. The Velocity Field in Basin	(83)
5.5.2. Response of the Surface and the Interface	(98)
5.6. Energy Distribution in Lake Melville	(116)
CHAPTER 6 : DISCUSSION	(122)
6.1. Introduction	(122)
6.2. General Discussion	(122)
6.3. Field Program	(125)
REFERENCES	(127)

List of Figures

-
- Figure 1.1 ; Location of Study Area (after Bobbitt and Akenhead, 1982) (2)
- Figure 1.2 ; Hamilton Inlet and Lake Melville (after Bobbitt and Akenhead) (3)
- Figure 1.3 ; Wind roses for Goose Bay Airport for various months. The numbers represent the mean wind speed in knots and the length of the vector is directly proportional to the directional frequency of the wind (after Kruger and Boucaud, 1963). (4)
- Figure 1.4 ; Location of sampling stations from which data were used (after Bobbitt and Akenhead, 1982). Abbreviations BB, I and BD refer to various expeditions (see text). (6)
- Figure 1.5 ; Plots of sigma-t versus depth for different stations (after Bobbitt and Akenhead, 1982) (7)
- Figure 1.6 ; Plots of salinity against depth for various stations in Lake Melville (after Bobbitt and Akenhead, 1982) (8)
- Figure 1.7 ; The unsmoothed bathymetry of Lake Melville in meters. The

numbers on the axes denote the grid locations. One grid length is 1.833 kilometers on both axes. (9)

Figure 3.1 ; The bathymetry of Lake Melville in meters after smoothing and suggested instrument mooring stations A and B (see Chapter 6). The numbers on the axes denote the grid locations. One grid length is 1.833 kilometers on both axes. (31)

Figure 3.2 ; Stream function Ψ for steady-state under a southwesterly wind of 7 m/s and a bottom stress coefficient of $K = 0.025/H \text{ sec}^{-1}$. The numbers on the axes denote the grid locations. One grid length is 1.833 kilometers on both axes. (33)

Figure 3.3 ; Stream function Ψ for steady-state under a westerly wind of 7 m/s and a bottom stress coefficient of $K = 0.01/H \text{ sec}^{-1}$. The numbers on the axes denote the grid locations. One grid length is 1.833 kilometers on both axes. (34)

Figure 3.4 ; Stream function Ψ for steady-state under a westerly wind of 7 m/s and a bottom stress coefficient of $K = 0.025/H \text{ sec}^{-1}$. The numbers on the axes denote the grid locations. One grid length is 1.833 kilometers on both axes. (35)

Figure 3.5 ; Stream function Ψ for steady-state under a westerly wind of 7 m/s and a bottom stress coefficient of $K = 0.05/H \text{ sec}^{-1}$. The numbers on the axes denote the grid locations. One grid length is 1.833 kilometers on both axes. (36)

Figure 3.6 ; Horizontal currents for steady-state under a westerly wind of 7 m/s

and a bottom stress coefficient of $K = 0.025/H \text{ sec}^{-1}$ (38)

Figure 4.1 ; (a) the staggered grid representation of variables ; (b) the grid square. (41)

Figure 4.2 ; Response of Lake Melville to wind forcing. The wind acts for four days or ninety-six hours from the west. (46)

Figure 4.3 ; Response of Lake Melville after wind cut-off at ninety-six hours from onset. Note that the scale has been changed in Figure 4.3(d) in order to better illustrate the currents. (50)

Figure 4.4 ; (a) Vorticity distribution associated with wind forcing in a basin ; (b) vorticity distribution in a basin after wind cut-off. (after Ocanady, 1982) (54)

Figure 4.5 ; Contours of surface elevation of Lake Melville in centimeters during and after the wind forcing episode. The wind cut-off is at ninety-six hours after onset. (all values multiplied by a factor of 100) (56)

Figure 4.6 ; Surface elevation at selected points at opposite ends of the lake as a function of time during the first twelve hours of wind forcing. (61)

Figure 4.7 ; Total energy in Lake Melville (in ergs) for different values of bottom stress coefficient K as a function of time. The arrow in each plot indicates the beginning of a "dip" (see text). (64)

Figure 4.8 ; Potential energy in Lake Melville (in ergs) as a function of time for different values of the bottom stress coefficient K during wind forcing only.

..... (65)

Figure 5.1 ; (a) The staggered grid representation of variables ; (b) the grid square.

..... (74)

Figure 5.2 ; Velocity field in the upper layer at various stages in the simulation.

..... (84)

Figure 5.3 ; (a) x-component of velocity at point (12,20) in the upper layer as a function of time ; (b) x-component of velocity at point (14,16) in the upper layer as a function of time ; (c) current hodograph at point (12,20); (d) current hodograph at point (14,16).

..... (89)

Figure 5.4 ; Velocity field in the lower layer at various stages in the simulation.

The wind cut-off is at twenty-four hours after onset. (93)

Figure 5.5 ; (a) x-component of velocity at point (12,20) in the lower layer as a function of time ; (b) x-component of velocity at point (14,16) in the lower layer as a function of time ; (c) current hodograph at point (12,20); (d) current hodograph at point (14,16).

..... (99)

Figure 5.6 ; Contours of surface elevation of Lake Melville at different stages in the simulation. (all values shown multiplied by a factor of 100) (102)

Figure 5.7 ; Surface elevation at selected points at the opposite ends of the lake
as a function of time during the first twelve hours of wind forcing.(108)

Figure 5.8 ; Contours of interfacial elevation of Lake Melville at various stages in
the simulation.(110)

Figure 5.9 ; Potential energy in each layer of Lake Melville (in ergs) as a function
of time.(117)

Figure 5.10 ; Kinetic energy in each layer of Lake Melville (in ergs) as a function
of time.(119)

Figure 5.11 ; Total energy distribution in Lake Melville (in ergs) as a function of
time.(121)

List of Tables

Table 3.1 ; Maximum value of current as a function of K (32)

Table 4.1 ; Spin-up and spin-down times of Lake Melville computed from the total energy in the model as a function of the bottom stress coefficient K (62)

Table 4.2 ; Spin-up times for an Ekman suction model of constant depth. D_E is the Ekman depth for Lake Melville of thirty-seven meters which has been used in computing the above times instead of the mean depth of eighty-six meters (see text below). (63)

CHAPTER 1 : INTRODUCTION

1.1. Background

Lake Melville, Labrador, is one of the three main water bodies making up Hamilton Inlet, the largest inlet along the Labrador coast. The other two water bodies are Groswater Bay and Goose Bay (Figure 1.1). As shown in Figure 1.2, the entrance to Hamilton Inlet consists of Groswater Bay which is about fifty kilometers in length and constricts into a narrow, shallow area averaging about 2.8 kilometers in width and thirty meters in depth with a length of twenty-two kilometers known as the Narrows. Before entering Lake Melville, the Narrows are divided into two channels by Henrietta Island and Eskimo Island (Figure 1.2).

Lake Melville lies to the west of the Narrows and has an average depth of about eighty-six meters. The sub-arctic climate of the Lake Melville area affects the circulation in terms of runoff and the presence of ice and is described by Krueger and Boucaud (1963) from data collected at Goose Bay Airport. The weather patterns of Goose Bay Airport have a tendency to alternate between those of maritime and continental climates, and the summer temperatures in the Goose Bay area tend to be comfortable but often cool. Winter is usually characterized by cold, crispy weather and rain, but midwinter thaws are not uncommon.

Figure 1.3 gives the wind roses for Goose Bay Airport. As can be seen, the dominant winds are the westerlies and the southwesterlies. These winds appear to be influenced by the northeast-southwest orientation of Hamilton Inlet and have a mean

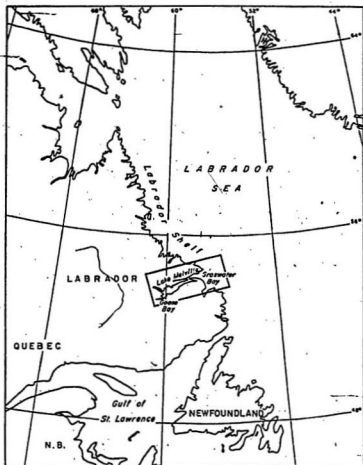
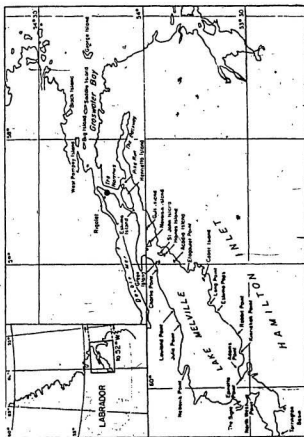


Figure 1.1 ; Location of Study Area (after Bobbitt and Akenhead, 1982)



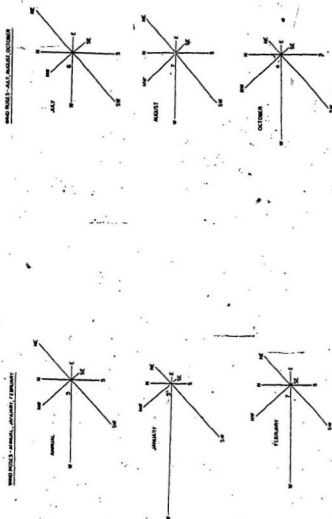


Figure 1.3 : Wind roses for Goose Bay Airport for various months. The numbers represent the mean wind speed in knots and the length of the vector is directly proportional to the directional frequency of the wind (after Kruger and Bouraud, 1983).

wind speed of about seven meters per second.

The majority of oceanographic data for Lake Melville were collected from 1949 to 1953 by the Blue Dolphin expeditions led by Captain David Nutt of Dartmouth College, New Hampshire. Salinity and temperature measurements were taken throughout Hamilton Inlet during summers in the years 1950 to 1953. In all, about 350 hydrographic samples were collected and the four major rivers were gauged to determine the amount of fresh water discharge into the lake. Additional data collected by the Fisheries Research Board of Canada in the late summer of 1952 aboard the vessel the Investigator II included the sampling of four stations in Lake Melville and one in Groswater Bay. The most recent field trip in the post-Churchill hydroelectric development period was carried out in August 1981 by the Department of Fisheries and Oceans aboard their vessel the Burin Bay. The positions of the stations sampled by the various expeditions are given in Figure 1.4. The density profiles for stations BB-4, BB-7, BD-52 and BD-47 are presented in Figure 1.5 and show that a two-layer structure of Lake Melville can be assumed with $\sigma_t = 9$ for the upper layer and $\sigma_t = 22$ for the lower layer. The salinity versus depth profiles (Figure 1.6) more clearly show a two-layer structure with the salinity of the upper layer (the epilimnion) being in the range three to five parts per thousand and the salinity of the lower layer (the hypolimnion) being in the range twenty to twenty-five parts per thousand. The thickness of the upper layer varies from ten to twenty meters. For this study, an upper layer thickness of fifteen meters has been taken. The bathymetry of Lake Melville is shown in Figure 1.7.

1.2. Motivation for the Present Study

Circulations in bodies of water as large as Lake Melville are of great interest from both the theoretical and practical points of view.

From a theoretical point of view, Lake Melville is of such a size that the effects of the earth's rotation are important to its dynamics, but at the same time not large

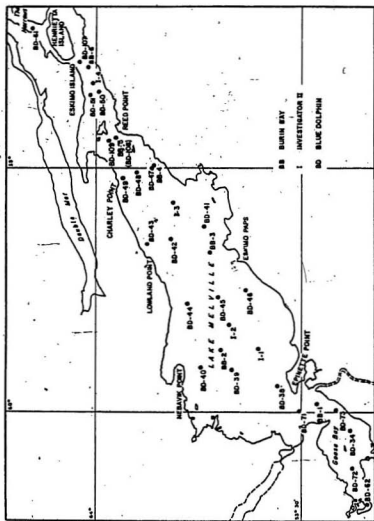


Figure 1.4 ; Location of sampling stations from which data were used (after Bobbitt and Akenhead, 1982). Abbreviations BB, I and BD refer to various expeditions (see text).

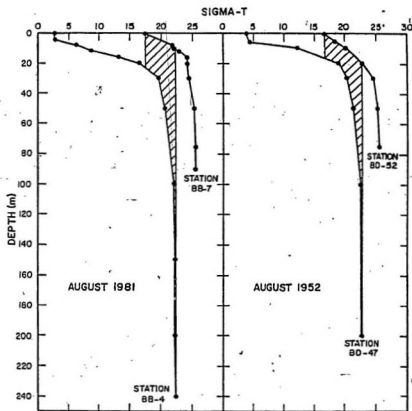


Figure 1.5 : Plots of sigma-t versus depth for different stations (after Bobbitt and Akenhead, 1982).

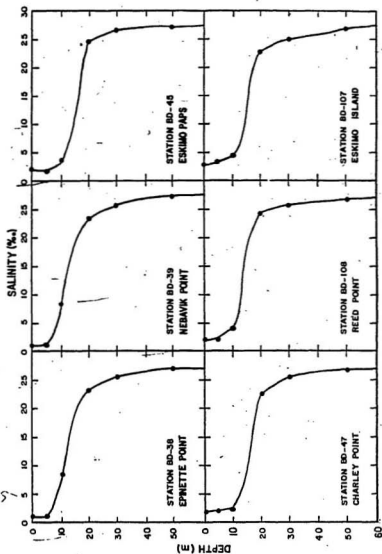


Figure 1.6 : Plots of salinity against depth for various stations in Lake Melville (after Bobbitt and Akenhead, 1982).

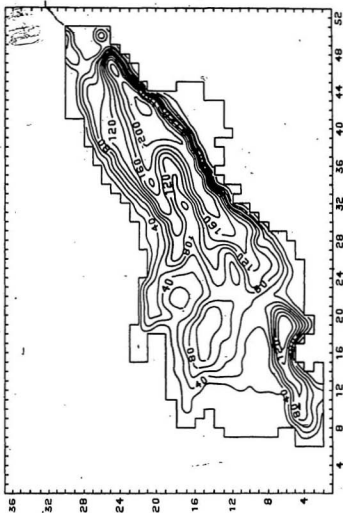


Figure 1.7 : The unsmoothed bathymetry of Lake Melville in meters. The numbers on the axes denote grid locations. One grid length is 1.833 kilometers on both axes.

enough to make the effects of the curvature of the earth's surface and the variation of the Coriolis parameter with latitude important factors. In addition, the lake is almost detached from the sea but still has a two-layer salinity and density structure. Other modelling of wind-driven circulations, especially in the Great Lakes, considered thermal stratification only, but Lake Melville is also strongly salinity stratified. It was interesting to see the effect of strong stratifications on simulations since models were generally adapted from the Great Lakes work.

On the practical side, a study of circulation in Lake Melville can help in the economic development of the area and associated navigational problems into the inland Labrador communities of Northwest River and Goose Bay. With industrial development currently taking place in this area, Port Labrador is being planned to service such developments. For this particular lake, modelling can help to shed light in this data-poor area by suggesting important circulation features and help plan field programs (see Chapter 6).

The construction of the hydroelectric development of the Churchill River began in 1967 and was completed in 1971. As a result, hundreds of existing lakes and hundreds of square kilometers of bog and muskeg were linked to form the Smallwood Reservoir from which water is released through various control systems. The increase in drainage area resulted in an increased and regulated freshwater inflow into Lake Melville. This increase in freshwater input has the potential for changing the water properties of this inshore water mass and local fishermen have for some time felt that the decrease in codfish stocks in the region since 1971 may be due in part to this hydroelectric development (Bobbitt and Akenhead, 1982). Further hydroelectric development in this area could introduce greater changes in the water properties of Lake Melville. In addition the formation of ice in the lake depends at least in part upon the water properties and a change in such properties of Lake Melville would probably change the patterns of freeze-up and affect winter season navigation.

1.3, General Factors of Circulation

The term 'fjord' is applied to an estuary or an inlet that has steep sides, a deep basin and a sill at the mouth, with a salinity distribution affected by a rather shallow surface layer which is appreciably diluted by fresh water runoff. Below this layer, the horizontal and the vertical salinity gradients are small. Since Lake Melville generally satisfies these criteria quite readily, some of its circulation features may be similar to basic fjord features.

Estuarine circulation is determined by the fresh water inflow and the mixing with seawater influenced by tidal currents. It is apparent (e.g. Ketchum, 1951; Pickard and Rodgers, 1959) that the wind can have an important influence on circulation and mixing as well. By exerting a stress on the surface of the lake, the wind as an external force can produce a net transport of water and the waves generated will increase the intensity of vertical mixing. The water transport in the surface layer will be mainly in the direction of the wind and hence, the normal seaward flow will be increased if the wind is blowing seawards along the estuary. The flow will be decreased or in some cases, reversed in direction if the wind blows in the opposite direction along the estuary.

External forces which cause water movements in lakes consist of changes in atmospheric pressure at the lake surface, the gravitational forces of the sun and the moon that generate tides, and of interest here, the wind or air currents blowing over the lake. Although the first three of the above mentioned factors will not be considered in this study, their importance in influencing circulation relative to the wind stress depends on each lake or basin under study. As far as the tidal influence from the sun and the moon is concerned, it would appear that it is directly proportional to the size of the basin in question. It is difficult to study such tidal oscillations in lakes since they exhibit very small tidal movements in the first place. Furthermore, in order to accurately determine the magnitude of the true tide, it would be necessary to somehow differentiate the tidal

oscillations from all the other mass fluctuations like internal and external seiches. As it turns out, the effect of tides is generally negligible on the circulation patterns in most lakes according to Harleman (1961). However, Lake Melville may behave as an Helmholtz oscillator (a quarter-wave resonator) with significant tidal forcing which occurs through the rises and falls of water levels at its entrance. There is some data on tidal levels in the lake (J. Bobbitt, personal communication) but it was not available for this study.

By far, the most important external current generating force in a lake is the wind. The wind affects the circulation in two ways. First, the air currents exert a shearing stress (the wind stress) at the air-water interface causing the water at the interface to accelerate. Viscous friction then causes the water layers deeper down to gain momentum. As a second consequence, the wind action on the surface of the lake causes the surface to oscillate and produces travelling waves. The velocity of the currents in a lake is related to the wind stress and does not depend on the waves directly, but, since the waves determine whether the lake surface is smooth or rough, they influence the wind stress on the lake surface and hence affect the efficiency with which a given wind produces currents. When the wind blowing over a lake reaches a certain critical speed, surface waves are generated. Munk (1947) has arrived at a value of seven meters per second for the critical wind speed. For winds blowing at a speed of greater than seven meters per second, surface waves are created and the lake surface becomes hydraulically rough, whereas for speeds of less than this critical wind speed the surface may be considered as smooth.

Since the wind that blows over a lake surface exerts a shearing stress on the surface of the water, the determination of the shearing stress τ from observed wind velocities \bar{W} has been undertaken by a large number of researchers. Most investigators have concluded that the wind stress varies as some power of the wind velocity relative to the water and is given by.

$$T = C_d \rho_a (W-V)^2 \quad (1.1)$$

where C_d is a drag coefficient, ρ_a is the density of the air, V is the velocity of the water at the lake surface, and W is the speed of the wind. In general, $|V| \ll |W|$, and the wind stress may be written as

$$T = C_d \rho_a (W)^2 \quad (1.2)$$

Taylor (1915) deduced that for turbulent air, $n=2$ and most researchers have arrived at the same or similar values of n . More recent observations by Large and Pond (1981) conclude that this quadratic wind stress law is quite valid for moderate or strong winds. Although values for the drag coefficient C_d have varied among different researchers, Wilson (1980) deduces that $C_d=0.002$ is a good value in accordance with the work of several researchers. Assuming $\rho_a=0.001$ grams per cubic centimeter as an average value for the density of air, the quadratic stress law for small to moderate wind speeds may now be written as

$$T = 2 \times 10^{-6} W^2 \quad (1.3)$$

which is valid for moderate to strong (including critical) wind speeds. Here, T is the surface stress in dynes per square centimeter and W is the wind speed in centimeters per second. This formula for the wind stress is to be used for the duration of this work.

In this thesis, no computations will be made for a divergent wind field. In view of the fact that the wind stress on the surface of Lake Melville is due mainly to the westerlies which have a much larger scale than the dimensions of the lake, a uniformity in the x and y directions is an adequate approximation for wind stress where steady-state circulation patterns are concerned, as shown by Rao and Murty (1970).

In general, lake currents can be separated into two categories : quasi-steady and time-dependent. In practice, no steady currents exist in a lake because of the time scale of the factors that cause currents to vary. However, it is true that there are periods during which the wind is varying sufficiently slowly so as to permit a steady-state analysis. Such an analysis gives rise to what are known as quasi-steady currents (referred to later in this work) and is appropriate if equilibrium can be attained. The shortest period oscillations of water flow are simple capillary waves. In deeper parts of the lake, capillary waves themselves are not significant as transporters of water, but when they reach shallow areas they change character from an orbital-type motion to a simple to and fro motion.

1.4. Scope of the Present Study

In this work, the study of the wind-induced circulation dynamics of Lake Melville revolves around three models : a steady-state homogeneous model, a time-dependent homogeneous model and a time-dependent two-layer model. A wind set-up lasting for four days is used for the time-dependent homogeneous model and one of a single day for the two-layer model. Typically, this wind period forms a standing wave called a 'seiche' which decays due to frictional effects after the wind is switched off.

Wind-induced circulation in shallow, homogeneous basins is governed by depth variations with the water transport running in the direction of the wind in shallow areas and against the wind in deeper areas (Csanady, 1982). A steady-state model is useful because it is the easiest one to implement and the resulting circulation pattern gives a good idea of the mean dynamic state of the lake in response to the average wind regime. Because the wind velocity varies somewhat on a day to day basis, it is possible that steady-state is not always reached, though upon a close examination the climatological and oceanographic records usually show quite consistent mean wind components and

persistent water movements at various locations in the Great Lakes (see Bennett, 1974).

Homogeneous time-dependent circulation models are also affected strongly by the bathymetry, and are probably more realistic than steady-state ones. Although applicable to many lakes (especially the Great Lakes) during the late fall, ice free periods in winter and early spring, these types of models are the next step up in terms of complexity.

A two-layer model of Lake Melville is by far, the most realistic one considered here, and also the most difficult one to implement. Since circulation in stratified basins is affected by the presence of internal waves like Kelvin waves alongshore and standing Poincare waves offshore (Simons, 1980), certain numerical instabilities can be induced which cause a degree of uncertainty in the simulations.

1.5. Results of the Work

There is a large amount of consistency in the results of the homogeneous models of Lake Melville. As is shown in chapters three and four, the circulation pattern resulting from the steady-state and time-dependent simulations of the homogeneous model appears to be in agreement with the physics of the problem at hand. The homogeneous models are very sensitive to the bottom stress specifications and the topography, factors which appear to be the most important in determining the circulation patterns in homogeneous lakes.

The two-layer model of Lake Melville discussed in chapter five is by far, the most realistic one. The simulations indicate that the baroclinic effects totally dominate the dynamics of the system. The effects of the topography of the lake appear to be small in determining the characteristics of the currents in most of the lake.

It is probable that in view of the lack of current measurements from the area, none of the models can be calibrated accurately enough to represent the magnitude of the

currents found at various points in the lake. The main objective of this thesis at this time therefore, is to determine the circulation pattern for Lake Melville by using homogeneous and two-layer models and make an attempt to deduce the approximate order of magnitude of the currents that may be found there.

CHAPTER 2 : THE HYDRODYNAMICAL EQUATIONS

OF MOTION AND CONTINUITY

2.1. General Equations for Barotropic Models

The following equations describe the time-averaged turbulent motion of a water body on a rotating earth (Proudman, 1953; Defant, 1961)

$$\frac{\partial u}{\partial t} + u \frac{\partial u}{\partial x} + v \frac{\partial u}{\partial y} + w \frac{\partial u}{\partial z} - f v = -\frac{1}{\rho} \frac{\partial p}{\partial x} + k \frac{\partial^2 u}{\partial z^2} + \Lambda \nabla^2 u \quad (2.1)$$

$$\frac{\partial v}{\partial t} + u \frac{\partial v}{\partial x} + v \frac{\partial v}{\partial y} + w \frac{\partial v}{\partial z} + f u = -\frac{1}{\rho} \frac{\partial p}{\partial y} + k \frac{\partial^2 v}{\partial z^2} + \Lambda \nabla^2 v \quad (2.2)$$

$$\frac{\partial w}{\partial t} + u \frac{\partial w}{\partial x} + v \frac{\partial w}{\partial y} + w \frac{\partial w}{\partial z} = -\frac{1}{\rho} \frac{\partial p}{\partial z} - g + k \frac{\partial^2 w}{\partial z^2} + \Lambda \nabla^2 w \quad (2.3)$$

where u , v and w are the velocity components in the x , y and z directions respectively with x positive eastwards, y positive northwards and z positive upwards and zero at the surface of the lake ; t is the time ; p is the local pressure ; f is the Coriolis parameter ; ρ is the fluid density ; k is the vertical eddy viscosity ; g is the acceleration due to gravity ; Λ is the the horizontal eddy viscosity (independent of position) and ∇^2 is the two-dimensional Laplacian. By considering the water in the basin to be incompressible, we use the continuity equation in the form

$$\frac{\partial u}{\partial x} + \frac{\partial v}{\partial y} + \frac{\partial w}{\partial z} = 0 \quad (2.4)$$

Dimensional analysis on equations (2.1) to (2.4) with the assumptions that

- (a) the hydrostatic approximation applies,
- (b) the wavelengths of the motion are large compared to the average depth so that the vertical accelerations are small (this follows from (a) above),
- (c) the non-linear accelerative terms are small i.e. the Rossby number $R_0 \ll 1$ (see Simons (1980), pg. 5),
- (d) the Coriolis parameter and the horizontal and vertical eddy viscosities are constant over the lake,

simplifies equations (2.1) to (2.4) to

$$\frac{\partial u}{\partial t} + fv = -\frac{1}{\rho} \frac{\partial p}{\partial x} + k \frac{\partial^2 u}{\partial z^2} \quad (2.5)$$

$$\frac{\partial v}{\partial t} + fu = -\frac{1}{\rho} \frac{\partial p}{\partial y} + k \frac{\partial^2 v}{\partial z^2} \quad (2.6)$$

$$\frac{\partial u}{\partial x} + \frac{\partial v}{\partial y} = -\frac{\partial w}{\partial z} \quad (2.7)$$

$$-\frac{1}{\rho} \frac{\partial p}{\partial z} - g = 0 \quad (2.8)$$

where the non-linear and the horizontal diffusive terms have been neglected. These describe motion in the horizontal plane only if we simplify equation (2.3) to the hydro-

tatic approximation (equation (2.8)) which requires only that $\frac{\partial w}{\partial t} \ll g$. Integration of equation (2.8) in the vertical gives an expression for the free surface pressure as

$$p(x, y, t) = p_a(x, y, t) + \rho g(\eta - z) \quad (2.9)$$

where $p_a(x, y, t)$ is the atmospheric pressure at the air-water interface and η is the surface elevation.

Let us now define the x and y components of volume transport as

$$M^{(x)} = \int_{-H}^{\eta} u \, dz, \quad M^{(y)} = \int_{-H}^{\eta} v \, dz, \quad (2.10)$$

the components of the vertically integrated velocity as

$$U = \frac{M^{(x)}}{H}, \quad V = \frac{M^{(y)}}{H}, \quad (2.11)$$

and the components of stress at a horizontal surface as

$$T^{(x)} = \rho k \frac{\partial u}{\partial z}, \quad T^{(y)} = \rho k \frac{\partial v}{\partial z}. \quad (2.12)$$

If we differentiate equation (2.9) with respect to the spatial coordinates, we get the forms

$$\frac{-1}{\rho} \nabla p = -g \nabla \eta, \quad \frac{-1}{\rho} \nabla p = -g \nabla \eta \quad (2.13)$$

which can be used to replace the pressure term from equations (2.5) and (2.6).

If we integrate equations (2.5) to (2.7) in the vertical (see Simons (1980), pg. 13) and use the definitions (2.11) and (2.12), we get the equations of volume transport

$$\frac{\partial M^{(x)}}{\partial t} - f M^{(y)} = -gH \frac{\partial \eta}{\partial x} + \frac{T_s^{(x)}}{\rho} - \frac{T_b^{(x)}}{\rho} \quad (2.14)$$

$$\frac{\partial M^{(y)}}{\partial t} + f M^{(x)} = -gH \frac{\partial \eta}{\partial y} + \frac{T_s^{(y)}}{\rho} - \frac{T_b^{(y)}}{\rho} \quad (2.15)$$

$$\frac{\partial M^{(x)}}{\partial x} + \frac{\partial M^{(y)}}{\partial y} = -\frac{\partial \eta}{\partial t} \quad (2.16)$$

after using the incompressibility condition. The deep water assumption

$$H + \eta \approx H$$

is used as well. In terms of the depth averaged current, equations (2.14) to (2.16) become

$$\frac{\partial U}{\partial t} - fV = -g \frac{\partial \eta}{\partial x} + \frac{T_s^{(x)}}{\rho H} - \frac{T_b^{(x)}}{\rho H} \quad (2.17)$$

$$\frac{\partial V}{\partial t} + fU = -g \frac{\partial \eta}{\partial y} + \frac{T_s^{(y)}}{\rho H} - \frac{T_b^{(y)}}{\rho H} \quad (2.18)$$

$$\frac{\partial(HU)}{\partial x} + \frac{\partial(HV)}{\partial y} = -\frac{\partial \eta}{\partial t} \quad (2.19)$$

As indicated in section 1.3, the surface stress is computed in accordance with the quadratic drag law, equation (1.4) for all three models considered here. The bottom stress

follows from the convention of Simons (1980) : If we use depth averaged velocity distribution, then it is possible to write the bottom stress as

$$\frac{\bar{\tau}_b}{\rho} = \bar{K} \bar{M} \quad (2.20)$$

where the various designations for \bar{K} are (Simons, 1980)

(1) linear : $\bar{K} = a/H$, $a=0.01$ to 0.05 cm/sec,

(2) quasi-linear : $\bar{K} = b/H^2$, $b \approx 100$ cm² / sec

(3) nonlinear : $\bar{K} = k |M| / H^2$, $k \approx 0.0025$

For all models of Lake Melville considered here, the linear definition of bottom stress was used only since it was established from test runs (not shown here) that the circulation is relatively unaffected by the other bottom stress specifications.

2.2. General Equations for the Baroclinic Model

The equations of hydrodynamics for a two-layer time-dependent system follow from equations (2.5) to (2.7). Let h and h' denote the depths of the upper and the lower layers respectively and assume that the densities are constant in each layer. The horizontal pressure gradients are now uniform within each layer and are given by

$$\nabla p = \rho g \nabla \eta, \quad \nabla p' = \rho' g \nabla \eta' - (\rho' - \rho) g \nabla h \quad (2.21)$$

where the unprimed and the primed quantities pertain to the upper and the lower

layers respectively. It follows from equations (2.5) to (2.8) that the vertically averaged equations for the upper layer (the epilimnion) are

$$\frac{\partial U}{\partial t} + fV = -g \frac{\partial \eta}{\partial x} + \frac{T_s(x)}{h\rho} - C_1(x) \frac{U - U'}{h\rho} \quad (2.22)$$

$$\frac{\partial V}{\partial t} + fU = -g \frac{\partial \eta}{\partial y} + \frac{T_s(y)}{h\rho} - C_1(y) \frac{V - V'}{h\rho} \quad (2.23)$$

$$\frac{\partial(\eta - \eta')}{\partial t} = -\frac{\partial(hU)}{\partial x} - \frac{\partial(hV)}{\partial y} \quad (2.24)$$

and the equations for the lower layer (the hypolimnion) are

$$\frac{\partial U'}{\partial t} + fV' = -g \frac{\bar{\rho}}{\rho'} \frac{\partial \eta}{\partial x} - g \left(1 - \frac{\rho}{\rho'}\right) \frac{\partial \eta'}{\partial x} + C_1(x) \frac{U - U'}{h' \rho'} - C_b(x) \frac{U'}{h' \rho'} \quad (2.25)$$

$$\frac{\partial V'}{\partial t} + fU' = -g \frac{\bar{\rho}}{\rho'} \frac{\partial \eta}{\partial y} - g \left(1 - \frac{\rho}{\rho'}\right) \frac{\partial \eta'}{\partial y} + C_1(y) \frac{V - V'}{h' \rho'} - C_b(y) \frac{V'}{h' \rho'} \quad (2.26)$$

$$\frac{\partial \eta'}{\partial t} = -\frac{\partial(h' U')}{\partial x} - \frac{\partial(h' V')}{\partial y} \quad (2.27)$$

where the interfacial and the bottom stress coefficients are given to a first approximation by (Bennett, 1978)

$$C_1 = \frac{0.001}{h} \text{ sec}^{-1} \quad (2.28)$$

$$C_b = \frac{0.02}{h'} \text{ sec}^{-1} \quad (2.29)$$

respectively. In order to simplify the analysis; it has been assumed that the surface and the interface displacements η and η' are small compared to both depths h and h' such that the approximations

$$h + \eta \approx h$$

and

$$h' + \eta' \approx h'$$

hold reasonably well in accordance with deep water theory.

2.3. Finite Difference Forms of Derivatives

Finite difference approximations to the derivatives were used to solve the equations of sections 2.1 and 2.2 numerically. Thus, the equations were reduced to their finite difference forms consisting of a standard five-point representation of the derivatives which follow from the Taylor Series expansions (Smith, 1965)

$$F(x + \Delta x) = F(x) + \frac{\Delta x}{(1!)} \frac{\partial F(x)}{\partial x} + \frac{\Delta x^2}{(2!)} \frac{\partial^2 F(x)}{\partial x^2} + \dots \quad (2.30)$$

$$F(x - \Delta x) = F(x) - \frac{\Delta x}{(1!)} \frac{\partial F(x)}{\partial x} + \frac{\Delta x^2}{(2!)} \frac{\partial^2 F(x)}{\partial x^2} - \dots \quad (2.31)$$

The central difference approximation to the spatial derivative was obtained by subtracting equation (2.31) from equation (2.30) with the result

$$\frac{\partial F(x)}{\partial x} = \frac{F(x + \Delta x) - F(x - \Delta x)}{2\Delta x} + O\left(\frac{\Delta x^2}{(3!)} \frac{\partial^3 F(x)}{\partial x^3}\right) \quad (2.32)$$

Rearrangements of equations (2.30) and (2.31) yielded the forward and backward

difference schemes given by

$$\frac{\partial F(x)}{\partial x} = \frac{(F(x + \Delta x) - F(x))}{\Delta x} + O\left(\frac{\Delta x}{2!} \frac{\partial^2 F(x)}{\partial x^2}\right) \quad (2.33)$$

$$\frac{\partial F(x)}{\partial x} = \frac{(F(x) - F(x - \Delta x))}{\Delta x} + O\left(\frac{\Delta x}{2!} \frac{\partial^2 F(x)}{\partial x^2}\right) \quad (2.34)$$

respectively. These approximations have an error term which is an order of Δx higher than the central difference approximations of equation (2.32).

Approximations to second-order derivatives follow by adding equations (2.30) and (2.31) and solving for the term $\frac{\partial^2 F(x)}{\partial x^2}$ with the resulting expression

$$\frac{\partial^2 F(x)}{\partial x^2} = \frac{1}{(\Delta x)^2} (F(x + \Delta x) - 2F(x) + F(x - \Delta x)) \quad (2.35)$$

The time derivatives were evaluated similarly for computational purposes. For numerical stability, different differencing schemes were used and the relevant schemes will be noted as they occur.

CHAPTER 3 : THE STEADY-STATE MODEL OF

LAKE MELVILLE

3.1. Derivation of the Stream Function Equation

For the steady-state model, no time-dependent terms are retained in the equations of volume transport (2.14) to (2.16) (Ramming and Kowalik, 1980) which now become

$$-f M^{(y)} = -gH \frac{\partial \eta}{\partial x} + \frac{T_s^{(x)}}{\rho} - \frac{T_b^{(x)}}{\rho} \quad (3.1)$$

$$f M^{(x)} = -gH \frac{\partial \eta}{\partial y} + \frac{T_s^{(y)}}{\rho} - \frac{T_b^{(y)}}{\rho} \quad (3.2)$$

$$\frac{\partial M^{(x)}}{\partial x} + \frac{\partial M^{(y)}}{\partial y} = 0 \quad (3.3)$$

in which the rigid-lid approximation is inherent since the time-dependent term $\frac{\partial \eta}{\partial t}$ vanishes from equation (3.3).

The specifications used for the wind stress \vec{T}_s and the bottom stress \vec{T}_b are as given by equations (1.3) and (2.20) respectively.


Since the continuity equation (3.3) requires that the divergence of the net horizontal volume flux vanish, $M^{(x)}$ and $M^{(y)}$ can be represented in terms of a stream function $\Psi(x,y)$ such that

$$M^{(x)} = -\frac{\partial \Psi}{\partial y}, \quad M^{(y)} = \frac{\partial \Psi}{\partial x} \quad (3.4)$$

Equations (3.4) were used to eliminate $M^{(x)}$ and $M^{(y)}$ from equations (3.1) to (3.3). After cross-differentiating equations (3.1) and (3.2) and eliminating the η terms, an equation representing the steady-state dynamics of Lake Melville and incorporating the linear bottom stress formulation (equation (2.20)) was arrived at after using the continuity equation (3.3) (Simons, 1980) :

$$H^2 \nabla \cdot \left[\frac{K}{H} \nabla \Psi \right] + fJ(H, \Psi) = H \left(\text{Curl } \vec{T}_t \right)_x + \frac{\partial H}{\partial y} T_t^{(x)} - \frac{\partial H}{\partial x} T_t^{(y)} \quad (3.5)$$

where



$$\nabla^2 \Psi = \frac{\partial^2 \Psi}{\partial x^2} + \frac{\partial^2 \Psi}{\partial y^2} \quad (3.6)$$

$$J(H, \Psi) = \frac{\partial H}{\partial x} \frac{\partial \Psi}{\partial y} - \frac{\partial H}{\partial y} \frac{\partial \Psi}{\partial x} \quad (3.7)$$

In equation (3.5) above, the latitudinal variation in the Coriolis parameter f given by

$$\beta = \frac{\partial f}{\partial y}$$

has been neglected. It is possible to do this if the horizontal dimensions of a lake are much smaller than the radius of the earth (Rao and Murty, 1970) which is the case with Lake Melville.

The components of the velocity field are computed by using the definitions

$$U = -\frac{1}{H} \frac{\partial \Psi}{\partial y}, \quad V = \frac{1}{H} \frac{\partial \Psi}{\partial x} \quad (3.8)$$

The wind stress forcing on the right hand side of equation (3.5) appears in the form of three separate terms. The first term on the right hand side, $(H \text{Curl } \vec{T}_s)_z$, is the vertical component of $\text{Curl } \vec{T}_s$, and depends on the curl of the wind stress field. The last two terms on the right hand side $\frac{\partial H}{\partial y} T_s^{(x)}$ and $\frac{\partial H}{\partial x} T_s^{(y)}$ depend essentially on the bottom configuration of the basin and may be referred to as the "bottom" slope component. Since the problem at hand is linear in terms of the stream function ψ , it may be expressed as

$$\psi = \psi_c + \psi_b \quad (3.9)$$

where ψ_c is the contribution from the curl of the wind field and ψ_b is the contribution from the bottom slope part. There can be other factors contributing to ψ such as precipitation, evaporation and drainage components. Such factors will be neglected for the duration of this work.

The appropriate boundary conditions follow from the requirement that the total transport normal to the boundary or the perimeter of the lake vanish (Pedlosky, 1979). This condition of no normal transport implies that ψ is a constant, or

$$\psi(x,y) = 0.$$

on the boundary.

3.2. Method of Solution

In the steady state stream function equation (3.5)

$$H^2 \nabla \cdot \left[\frac{\vec{K}}{H} \nabla \psi \right] + fJ(H, \psi) = \frac{\partial H}{\partial y} T_s^{(x)} - \frac{\partial H}{\partial x} T_s^{(y)} + H (\text{Curl } \vec{T}_s)_z$$

the last term on the right hand side vanishes for a constant wind stress that is used in

all the simulations in this paper. Using the linear formulation of the bottom stress coefficient K (see section 2.1), we may write the first term of the left hand side of equation (3.9) as

$$H^2 \nabla \left(\frac{K}{H} \nabla \psi \right) = H^2 \nabla \left(\frac{a}{H^2} \nabla \psi \right) = a (\nabla^2 \psi - \frac{2}{H} \nabla H \cdot \nabla \psi) \quad (3.10)$$

Equation (3.8) now becomes

$$\nabla^2 \psi - \frac{2}{H} \nabla H \cdot \nabla \psi + \frac{f}{a} J(H, \psi) = \frac{\partial H}{\partial y} \frac{T_s^{(u)}}{a} - \frac{\partial H}{\partial x} \frac{T_s^{(v)}}{a} \quad (3.11)$$

After multiplying through by the square of the grid spacing δ^2 and expanding the Jacobian terms and collecting the various terms, we end up with the form

$$\begin{aligned} \delta^2 \nabla^2 \psi - \left(\frac{2}{H} \delta \frac{\partial H}{\partial x} + f \frac{\delta}{a} \frac{\partial H}{\partial y} \right) \frac{\partial \psi}{\partial x} \delta \\ - \left(\frac{2}{H} \delta \frac{\partial H}{\partial y} - f \frac{\delta}{a} \frac{\partial H}{\partial x} \right) \frac{\partial \psi}{\partial y} \delta \\ + \frac{\delta^2}{a} \frac{\partial H}{\partial x} T_s^{(v)} - \frac{\delta^2}{a} \frac{\partial H}{\partial y} T_s^{(u)} = 0. \end{aligned} \quad (3.12)$$

If we define the following,

$$CC(x, y) = 2 \frac{\delta}{H} \frac{\partial H}{\partial x} + f \frac{\delta}{a} \frac{\partial H}{\partial y} \quad (3.13)$$

$$DD(x, y) = 2 \frac{\delta}{H} \frac{\partial H}{\partial y} - f \frac{\delta}{a} \frac{\partial H}{\partial x}$$

$$F(x, y) = \frac{\delta^2}{a} \frac{\partial H}{\partial x} T_s^{(v)} - \frac{\delta^2}{a} \frac{\partial H}{\partial y} T_s^{(u)}$$

then equation (3.12) can be written conveniently as

$$\delta^2 \nabla^2 \psi - CC(x,y) \left[\delta \frac{\partial \psi}{\partial x} \right] - DD(x,y) \left[\delta \frac{\partial \psi}{\partial y} \right] + F(x,y) = 0. \quad (3.14)$$

The grid used for computations in this model is a single-lattice symmetrical grid (see Ramming and Kowalik (1980), page 115). Although it is conventional to use central differences in evaluating such equations, these often give poor convergences. In equation (3.14), terms like $CC(x,y)$ and $DD(x,y)$ seem to act like advection terms (T.J. Simons, personal communication) and conventional finite difference schemes are often inadequate in dealing with the advection of variables that have steep gradients. Therefore, to help the solution converge, such terms of equation (3.12) are treated as follows in the finite difference scheme;

$$\text{for } CC(x,y) > 0; \delta \frac{\partial \psi}{\partial x} = \psi(I,J) - \psi(I,J-1)$$

$$\text{for } CC(x,y) < 0; \delta \frac{\partial \psi}{\partial x} = \psi(I,J+1) - \psi(I,J)$$

$$\text{for } DD(x,y) > 0; \delta \frac{\partial \psi}{\partial y} = \psi(I,J) - \psi(I-1,J)$$

$$\text{for } DD(x,y) < 0; \delta \frac{\partial \psi}{\partial y} = \psi(I+1,J) - \psi(I,J)$$

where δ is the grid spacing (uniform in both the x and y directions) and I and J are the spatial coordinates in the y and x directions respectively in the grid. The other derivatives were evaluated using central differences and the convergence was eased by the process of successive over-relaxation of the finite difference scheme (Simons, 1980).

3.3. The Input Data

The bathymetric data for Lake Melville were obtained from Canadian Hydrographic Service chart number 5142 with scale 1:100000. A grid of mesh size 1.9 centimeters corresponding to a spacing of 1.833 kilometers was drawn over the chart and the depths H_{ij} read off at all the interior points of the lake. At the boundary and land points, H_{ij} was set equal to zero and the small islands at the northeastern end of the lake were deleted. In order to eliminate computational instabilities that might arise from shallow depths within the domain of integration, all depths that were greater than zero but less than twenty-five meters were set equal to twenty-five meters. The whole depth profile (as presented in Figure 1.7) was then smoothed by using the formula (Rao and Murty, 1970)

$$H_{ij} = (H_{i+1,j} + H_{i-1,j} + H_{i,j+1} + H_{i,j-1} + 4H_{ij}) / 8. \quad (3.15)$$

This procedure left most of the depths over the lake relatively unaffected.

The smoothed depth profile of Lake Melville is given in Figure 3.1 and has a contour interval of twenty meters. The deepest part of the lake is in the northeastern section, whereas the shallowest part is on the western side. The depth gradients are much greater along the northeastern lower shore than anywhere else, and in fact the whole northeastern half of the lake is quite deep with some depths exceeding 200 meters. It will be shown that such a depth profile exerts a strong influence on the circulation pattern.

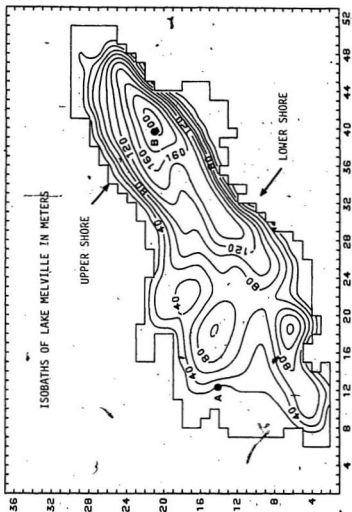


Figure 3.1 : The bathymetry of Lake Melville in meters after smoothing and suggested instrument mooring stations A and B (see Chapter 6). The numbers on the axes denote grid locations. One grid length is 1.833 kilometers on both axes.

3.4. The Results of the Model

Meteorological data for the period 1955 to 1980 from Goose Bay Airport indicate that the two most common winds are the westerlies and the southwesterlies. In view of the available meteorological data, a wind speed of seven meters per second corresponding to wind stress of about one dyne per square centimeter was chosen for all the simulations.

Figure 3.2 shows the stream function contours for a southwesterly wind and Figures 3.3 to 3.5 illustrate the circulation pattern for a westerly wind. For the same value of the bottom stress coefficient $K = 0.025 / H \text{ sec}^{-1}$, it is apparent from Figures 3.2 and 3.4 that these two wind directions give essentially the same overall circulation pattern. In view of this, a westerly wind was chosen for all subsequent calculations.

The bottom stress coefficient K ranges in value from $0.01 / H \text{ sec}^{-1}$ to $0.05 / H \text{ sec}^{-1}$ for the Great Lakes (Simons, 1980). A value of $0.025 / H \text{ sec}^{-1}$ was chosen as a reference in order to see what effect, if any, was created on the circulation pattern by different values of this skin coefficient. As is clear from Figures 3.3 to 3.5, the different values of K had virtually no effect on the position of the gyres in Lake Melville, although a change in the value of this bottom stress coefficient did affect the stream function values and hence the current values directly. Table 3.1 shows the affect of different values of K on the maximum computed current.

$K \text{ (sec}^{-1}\text{)}$	Maximum Total Current in cm/sec
0.01/H	19.00
0.025/H	14.05
0.05/H	9.37

Table 3.1 : Maximum value of current as a function of K

In view of the lack of field data from the area, a particular value of K cannot be determined from the simulation results and hence, the precise magnitude of the currents can

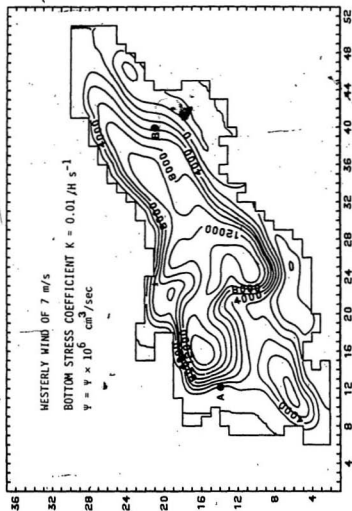


Figure 3.3 ; Stream function ψ for steady-state under a westerly wind of 7 m/s and a bottom stress coefficient of $K = 0.01/H \text{ sec}^{-1}$. The numbers on the axes denote grid locations. Of grid length is 1.833 kilometers on both axes.

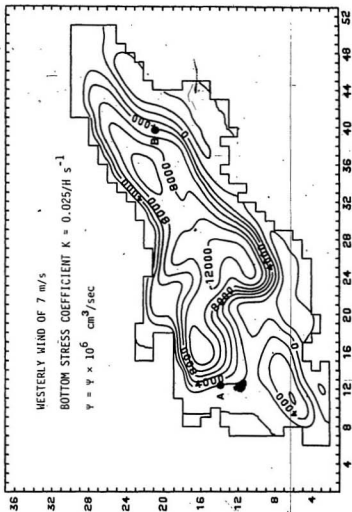


Figure 3.4 : Stream function ψ for steady-state under a westerly wind of 7 m/s and a bottom stress coefficient of $K = 0.025/H \text{ sec}^{-1}$. The numbers on the axes denote grid locations. One grid length is 1.833 kilometers on both axes.

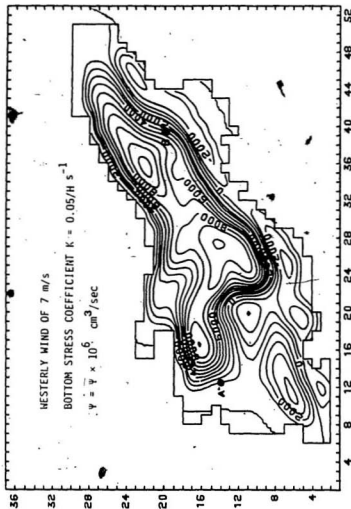


Figure 3.5 : Stream function ψ for steady-state under a westerly wind of 7 m/s and a bottom stress coefficient of $K = 0.05/H \text{ sec}^{-1}$. The numbers on the axes denote grid locations. One grid length is 1.833 kilometers on both axes.

not be the primary concern. However, the second value in Table 3.1 (above) gives maximum currents of an order of magnitude similar to those found in the Great Lakes and may be the most appropriate one.

The circulation pattern consists of one main gyre covering most of the lake and a smaller gyre in the western part which is considerably smaller than the main one. There is also some evidence of a third gyre along the lower shore of Lake Melville which is narrow and elongated. The main gyre rotates clockwise as does the one in the western end. The gyre along the lower shore of the lake has an anti-clockwise sense of rotation. The lack of field data does not allow any verification of these results, however communication with a local fisherman indicates that the currents in Lake Melville are consistent with these results (private communication with Mr. M. Best).

Comparison of Figure 3.1 with Figures 3.2 to 3.5 illustrates just how remarkably the streamline pattern is determined by the depth profile since the relative directions of the currents follow from the approximate balance between the total gravity force $gh \nabla \eta$ due to the surface slope and the local wind stress because the Coriolis term is relatively small. Since the total gravity force is directly proportional to the local depth, it is small in shallow areas compared to the wind stress and the less mass here affected by the same wind stress causes the shallow water currents to be higher than in deep water. The formation of the convergence and divergence zones due to the Ekman transport near the lower and the upper shores respectively also contributes to this. However in deep water, the pressure gradient dominates because of the Coriolis term being small and a return flow is evident (Figure 3.6) which is typically weaker than the coastal currents. Such a pressure gradient results also from the wind setups at the downwind end of the lake, as well as from some accumulations from Ekman transports to the right of the wind (in the northern hemisphere). Thus the currents are larger and in the direction of the wind in shallow areas, but smaller and against the wind in deep water (Figure 3.6).

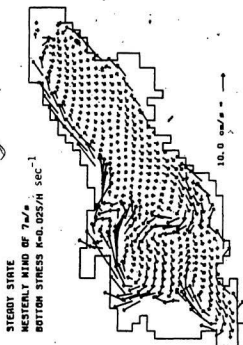


Figure 3.6 ; Horizontal currents for steady-state under a westerly wind of 7 m/s and a bottom stress coefficient of $K = 0.025/H \text{ sec}^{-1}$.

CHAPTER 4 : THE TIME-DEPENDENT BAROTROPIC

MODEL OF LAKE MELVILLE

4.1. Introduction

A time-dependent homogeneous model of Lake Melville is the next step-up in terms of complexity and helps one understand the time response of the lake as a function of atmospheric forcing. For this particular model, the stream function approach was found to present numerical difficulties like a 'numerical drift' in the Gauss-Seidel iteration procedure used. In order to reduce such errors, a solution based on the time integration of the finite-difference forms of the primitive equations was chosen. An examination of the energetics of the system helps in identifying the dynamic mechanisms responsible for the variations and fluctuations in the lake properties which tell us how and when the model approaches steady-state. This model is a free surface one which means that the surface gravity waves are present in this model as opposed to the steady-state model of Chapter 3 in which they are not. The equations of volume transport for such a homogeneous system are given by equations (2.14) to (2.16).

4.2. Total Circulation Energy for Homogeneous Basins

Motions in lakes can be better displayed if the amount of energy contained in the circulation is investigated. In particular, the spin-up and spin-down times can be deduced from these energy considerations and certain basic oscillations examined.

The total potential energy in a homogeneous basin is given by the area integral

$$P.E. = \int_A \frac{\rho}{2} \eta^2 dA \quad (4.1)$$

and the total kinetic energy is given by the volume integral

$$K.E. = \int_V \frac{\rho}{2} [U^2 + V^2] dV. \quad (4.2)$$

The total energy in the lake may be expressed as the sum of the total kinetic energy and the total potential energy, or

$$\text{Total Energy} = \int_A \frac{\rho}{2} \eta^2 dA + \int_V \frac{\rho}{2} [U^2 + V^2] dV \quad (4.3)$$

where these integrals are evaluated numerically.

4.3. The Method of Solution

4.3.1. The Staggered Grid

The variables are defined on a staggered grid representation of the Richardson-type and their relative positions for computational purposes are shown in Figure 4.1. The hydrodynamical equations of volume transport are evaluated at time steps $T\Delta t$ where $T = 0, 1, 2, 3, \dots$ and Δt is the time step. For the grid, the mesh size is taken to be the same in the x and y directions, i.e.

$$\Delta x = \Delta y = \delta = 1.833 \text{ kilometers}$$

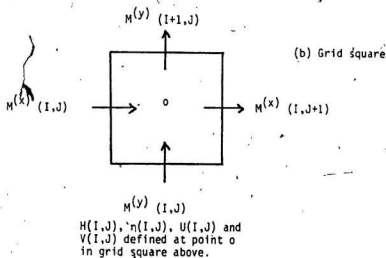
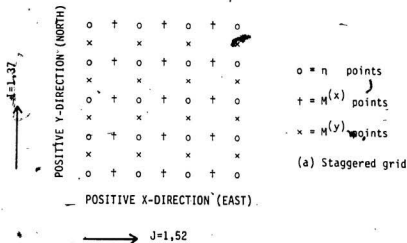


Figure 4.1 : (a) the staggered grid representation of variables; (b) the grid square.

4.3.2. The Boundary and Initial Conditions

The wind is turned on at time $t = 0$ and the initial conditions

$$\eta(x,y,t) = M^{(x)}(x,y,t) = M^{(y)}(x,y,t) = 0 \text{ for } t \leq 0$$

are used. Since we require that the component of volume transport normal to the boundary be vanishing, the boundary condition

$$\bar{M}(x,y)_{\text{normal}} = 0 \text{ on the boundary}$$

is used for all t .

4.3.3. Numerical Solution of the Equations

The time step in this model is restricted by the Courant-Friedrichs-Levy criterion which requires that the inequality (Simons, 1980)

$$\Delta t \leq \frac{\delta}{\sqrt{2gH_{\max}}} \quad (4.4)$$

be satisfied for numerical stability. For Lake Melville, the largest time step that can be used is about forty seconds. As a matter of convenience, a time step of thirty seconds was selected.

All derivatives are evaluated here using forward differences. The time extrapolation proceeds by predicting the surface elevation η first and then the velocity components by utilizing the most recent previously computed value of each variable (Simons, 1982).

4.3.4. Prediction of the Surface Elevation

The finite difference form of the continuity equation (2.16) using forward differences is found to be

$$\frac{1}{\Delta t}[\eta^i + \Delta t - \eta^i] = \frac{-1}{\delta}[M^{(x)}(I, J+1) - M^{(x)}(I, J)]^i - \frac{1}{\delta}[M^{(y)}(I+1, J) - M^{(y)}(I, J)]^i \quad (4.5)$$

Rearrangement of this equation yields the form

$$\begin{aligned} \eta^i + \Delta t &= \eta^i \\ &- \frac{\Delta t}{\delta}[M^{(x)}(I, J+1) - M^{(x)}(I, J)]^i \\ &+ M^{(y)}(I+1, J) - M^{(y)}(I, J)]^i \end{aligned} \quad (4.6)$$

which is iterable in time.

4.3.5. Prediction of the Mass Transport Components

The momentum equation in the x-direction, equation (2.14) can be written in its finite-difference form as

$$\begin{aligned} \frac{1}{\Delta t}[M^{(x)}(I, J)^i + \Delta t - M^{(x)}(I, J)^i] &= [f M^{(y)}(I, J)]^i \\ &- \frac{gH}{\delta}[\eta(I, J-1) - \eta(I, J)]^i + \Delta t \\ &- [KM^{(x)}(I, J)]^i + [T_s^{(x)}]^i \end{aligned} \quad (4.7)$$

Upon rearrangement, this equation becomes

$$\begin{aligned} M^{(x)}(I, J)^i + \Delta t &= M^{(x)}(I, J)^i + \Delta t[f M^{(y)}(I, J)]^i \\ &+ \Delta t \frac{gH}{\delta}[\eta(I, J-1) - \eta(I, J)]^i + \Delta t \\ &- \Delta t[KM^{(x)}(I, J)]^i + \Delta t[T_s^{(x)}]^i \end{aligned} \quad (4.8)$$

As is clear from Figure 4.1, the x and y components of volume transport are computed on the adjacent sides of the grid square. In order to use equation (4.8), we must first compute the y component of volume transport at the same point by using the simple averaging formula

$$M^{(y)}(I,J)^i = \frac{1}{4} [M^{(y)}(I,J-1) + M^{(y)}(I+1,J-1) + M^{(y)}(I,J) + M^{(y)}(I+1,J)]^i \quad (4.9)$$

before computing the value of $M^{(x)}(I,J)^{i+\Delta t}$.

The y component of volume transport is computed in a similar way. The finite difference form of the momentum equation in the y-direction, equation (2.15) is found to be

$$\begin{aligned} \frac{1}{\Delta t} [M^{(y)}(I,J)^{i+\Delta t} - M^{(y)}(I,J)^i] &= -[f M^{(x)}(I,J)]^i + \Delta t \\ &\quad - \frac{gH}{\delta} [\eta(I-1,J) - \eta(I,J)]^i + \Delta t \\ &\quad - [KM^{(y)}(I,J)]^i + [T_e^{(y)}]^i \end{aligned} \quad (4.10)$$

Rearrangement of this equation yields the form

$$\begin{aligned} M^{(y)}(I,J)^{i+\Delta t} &= M^{(y)}(I,J)^i - \Delta t [f M^{(x)}(I,J)]^i + \Delta t \\ &\quad - \Delta t \frac{gH}{\delta} [\eta(I-1,J) - \eta(I,J)]^i + \Delta t \\ &\quad - \Delta t [KM^{(y)}(I,J)]^i + \Delta t [T_e^{(y)}]^i \end{aligned} \quad (4.11)$$

Because the x component of volume transport is evaluated at a different point relative to the y component, an averaging formula of the type

$$M^{(x)}(I,J)^i + \Delta t = \frac{1}{4} [M^{(x)}(I-1,J) + M^{(x)}(I,J) + M^{(x)}(I,J+1) + M^{(x)}(I+1,J)]^i \quad (4.12)$$

$$+ M^{(3)}(I-1, J+1) + M^{(3)}(I, J+1)]^2 + \Delta t$$

must be used to compute the value of $M^{(3)}(I, J)$ to be used in conjunction with equation (4.11) above.

4.4. Results of the Time-Dependent Model

4.4.1. Response of Lake Melville to Wind Forcing

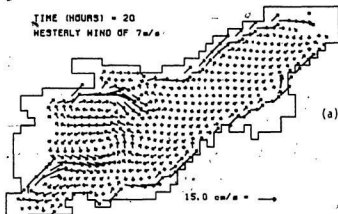
The current vector diagrams of Lake Melville are shown from the onset of the wind at time $t = 0$ to near its cut-off after ninety-six hours in Figure 4.2. The current pattern closely resembles Figure 3.6, especially from forty hours and onwards. From the discussion in section 3.4.2 then, in around forty hours the model approaches steady-state where the depth contours determine the magnitude of the currents. As is clear from these figures, the circulation pattern changes little throughout the forcing period. Currents are simulated as running downwind along the upper and the lower shores and upwind in the interior of the lake. The response of the currents to the wind in the shallow regions (i.e. along the shores) appears to be faster than the response in the deeper areas. For this time-dependent homogeneous model, the currents near the shore constituting a 'coastal jet' phenomena are part of what is known as the 'quasi-static response' or a 'persistent flow'. This is especially dominant near the shores during forcing and is due to the formation of the convergence and divergence zones due to Ekman transport. Evidence of this is found in Figures 4.2(a) to 4.2(d) where the circulation pattern adjusts to wind forcing in the interior of the lake (i.e. in the deeper areas) later than it does in shallow areas, near the coast.

The basic circulation pattern consists of two main gyres in the upper and the lower parts of the lake. The upper gyre has a clockwise sense of rotation and covers most of

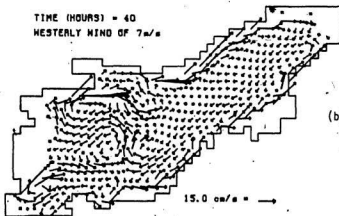
A

Figure 4.2 ; Response of Lake Melville to wind forcing. The wind acts for four days or ninety-six hours from the west.

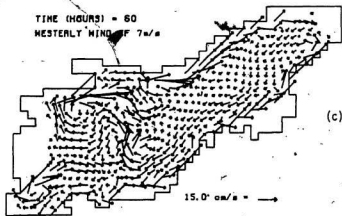
TIME (HOURS) = 20
WESTERLY WIND OF 7m/s



TIME (HOURS) = 40
WESTERLY WIND OF 7m/s

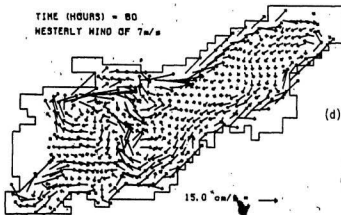


TIME (HOURS) = 60
WESTERLY WIND OF 7 m/s



(c)

TIME (HOURS) = 80
WESTERLY WIND OF 7 m/s



(d)

the basin with the return flow centered along the talweg (the line joining the deepest points along the longitudinal axis of the lake) of the lake where the pressure gradient dominates over the wind stress. The lower gyre is narrow and elongated and has an anti-clockwise sense of rotation. Again, the return flow for this gyre (as for the upper one) is along the talweg of the lake. A couple of much smaller anticyclonic gyres can be seen at the western end of the lake which probably arise from higher order effects, however these gyres also show up in the steady-state model (Figures 3.1 to 3.5). The location and sense of the largest gyres though, is consistent with the bathymetry of the lake (Figure 3.1) (as for the steady-state model) in that they are centered around the areas of the largest depth gradients.

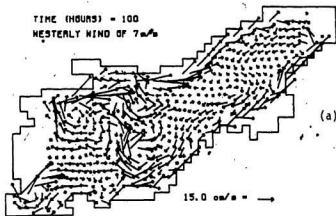
4.4.2. Response of Lake Melville after wind cut-off

After ninety-six hours (or four days) of wind forcing, model wind stress is cut off and the spin-down response of the lake of begins. By this time, the lake had reached equilibrium for a bottom stress coefficient of $K = \frac{0.025}{H} \text{ sec}^{-1}$ (see Table 4.1).

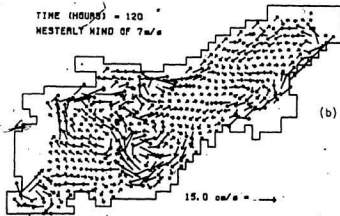
Figure 4.3 illustrates the decay of the circulation pattern. Along both the upper and the lower shores of the lake, some evidence of current weakening and subsequent reversal is apparent one day after wind cut-off (Figure 4.3(b)), though the current pattern over the rest of the lake does not respond as rapidly as this. Beyond a day after wind cut-off (Figure 4.3(b)), the rest of the basin starts to respond and large scale current reversals are apparent especially along the shores which lead to eddy formation in both ends of the lake. These drift somewhat with time, and their formation and behaviour can be explained from the point of view of the conservation of potential vorticity which is given by the equation

Figure 4.3 ; Response of Lake Melville after wind cut-off at ninety-six hours after onset. Note that the scale has been changed in Figure 4.3(d) in order to better illustrate the currents.

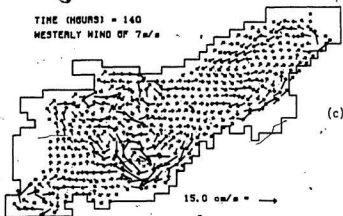
TIME (HOURS) = 100
WESTERLY WIND OF 7 m/s



TIME (HOURS) = 120
WESTERLY WIND OF 7 m/s

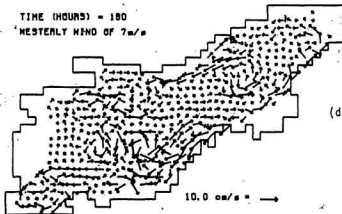


TIME (HOURS) = 140
WESTERLY WIND OF 7 m/s



(c)

TIME (HOURS) = 180
WESTERLY WIND OF 7 m/s



(d)

$$\begin{aligned} \frac{\partial \zeta}{\partial t} = \frac{\partial}{\partial t} \left(\frac{\partial M^{(y)}}{\partial x} - \frac{\partial M^{(x)}}{\partial y} \right) = & r \frac{\partial \eta}{\partial t} \\ & - g \left(\frac{\partial H}{\partial x} \frac{\partial \eta}{\partial y} - \frac{\partial H}{\partial y} \frac{\partial \eta}{\partial x} \right) \\ & + \frac{\partial F_y}{\partial x} - \frac{\partial F_x}{\partial y} \end{aligned} \quad (4.13)$$

where ζ denotes the vorticity and F_x and F_y are the x and y components of the net horizontal stress. The vorticity distribution in the basin is illustrated in Figure 4.4 both during and after wind forcing episodes. During the wind forcing episode, the fluid crosses the depth contours in the downwind or the far end moving from the shallow regions of the basin to deeper ones. This action contributes to the corresponding stretching of the vortex lines and produces the positive sign on the left hand side of this equation (4.13). As a result, a positive depth integrated vorticity results at the far end of the lake. At the upwind end of the lake, a negative vorticity is generated in a like manner because the fluid is forced from deep to shallow parts of the lake. Such a mode of motion is part of what can be best described as a 'vorticity wave' which is not propagating when the wind is steady. This type of a wave depends for its existence on depth variations and the earth's rotation and is related to the vortex stretching phenomena. By the stretching of vortex lines on a rotating earth therefore, cyclonic vorticity is generated at the downwind end and anticyclonic vorticity at the upwind end. At the far end of the lake, the vorticity is increased to the right of the talweg and decreased to the left because of the contribution of the planetary vorticity (the Coriolis effect) to this wind-induced vorticity. The change of vorticity here is positive on both sides of the talweg. At the upwind end of the lake, the opposite occurs with the vorticity being strengthened to the left side of the talweg and weakened to the right of it. Therefore, on the left of the talweg the vorticity was originally negative so it will first weaken and then change sign, but on the right hand side, the vorticity was already positive, so it will strengthen. Now the line that separates the cyclonic and the anticyclonic vorticities (which initially

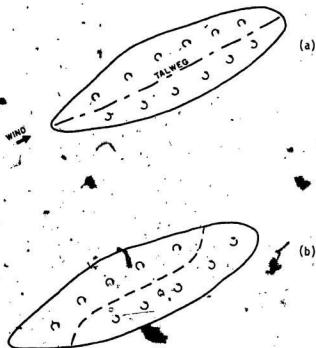


Figure 4.4 : (a) Vorticity distribution associated with wind forcing in a basin ; (b) vorticity distribution in a basin after wind cut-off. (after Csanady, 1982)

coincides with the talweg, Figure 4.4(a)) begins to rotate counter-clockwise, or in other words, the gyre pattern of the lake starts to rotate cyclonically under the influence of the Coriolis parameter after the wind is switched off until a short time later, the pattern appears as that shown in Figure 4.4(b). In the case of Lake Melville, such a rotation is not more obvious because of the dissipative effects of bottom friction.

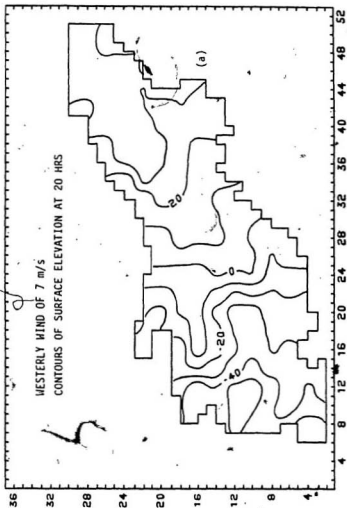
The behaviour of the free surface of Lake Melville is illustrated in Figure 4.5. During the period of wind forcing (Figures 4.5(a) to 4.5(c)) the water starts to pile up at the eastern end of the lake as indicated by the positive values of the surface elevation here. At the western end of the lake, the opposite is true, and the surface elevation is lowered. As the wind forcing progresses, the rotational effect of the earth causes water piled up at the eastern end to move southwards. These effects are small since the Coriolis parameter exerts little influence in narrow, elongated basins that typically have a maximum width of less than one Rossby radius such as Lake Melville. The rotational behaviour of a more circular basin would be more obvious.

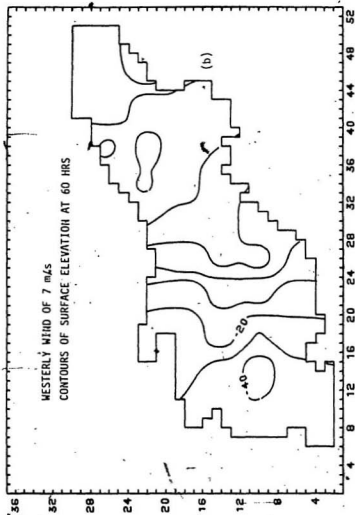
Figure 4.6 shows a plot of surface elevation as a function of time at two selected points diametrically opposite to each other and at the opposite ends of the lake. The oscillations are 180 degrees out of phase with respect to each other. The external (or the barotropic) Kelvin wave (see Canady, 1967) is apparent from the oscillations in this plot which have a period of a little over 1.5 hours. This is in good agreement with first order calculations (for $n=1$) which also yield a period of slightly over 1.5 hours using the Merian formula

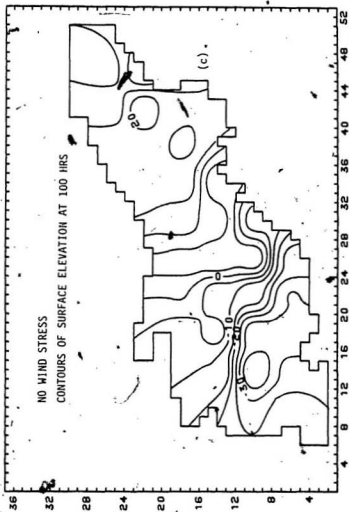
$$T = \frac{2L}{\sqrt{gH}n}, \text{ where } n=1,2,3,\dots \quad (4.14)$$

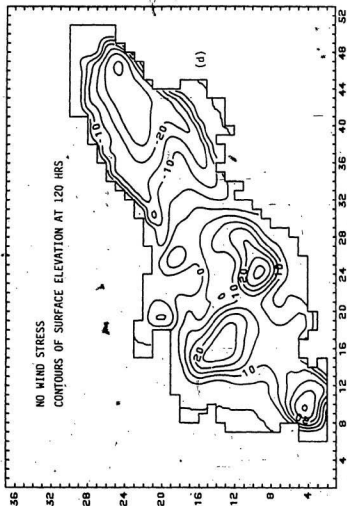
where L is the length of the lake of approximately ninety-five kilometers and H is the average depth of Lake Melville of about eighty-six meters. In this particular case, the barotropic Kelvin wave travels up and down the lake with a phase speed of a surface

Figure 4.5 ; Contours of surface elevation of Lake Melville in centimeters during and after the wind forcing episode. The wind cut-off is at ninety-six hours after onset. (all values multiplied by a factor of 100)









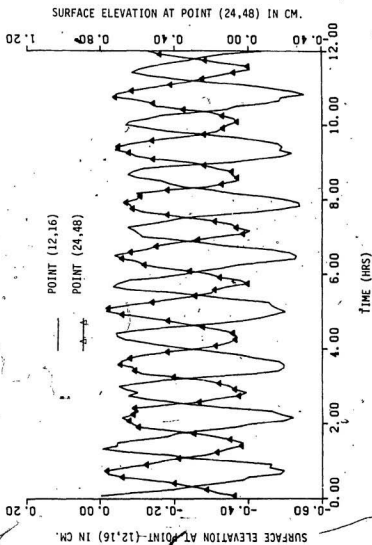


Figure 4.0 : Surface elevation at selected points at opposite ends of the lake as a function of time during the first twelve hours of wind forcing.

gravity wave given by

$$C = \sqrt{g H} \quad (4.15)$$

(where H is the average depth of Lake Melville of eighty-six meters). The 'fine structure' of the peaks may be due to higher order barotropic Kelvin wave oscillations (i.e., for $n > 1$) in the basin.

4.5. Energy Considerations

A reasonably good idea of the spin-up and spin-down times of Lake Melville can be obtained from the energy considerations. Three values of the bottom stress coefficient were considered and the response times deduced by taking the e-folding time. The values are tabulated below;

$K \text{ (sec}^{-1}\text{)}$	Spin-up time (hours)	Spin-down time (hours)
$0.01/H$	72	93
$0.025/H$	45	38
$0.05/H$	25	25

Table 4.1 : Spin-up and spin-down times of Lake Melville computed from the total energy in the model as a function of the bottom stress coefficient K .

The spin-up and spin-down times vary inversely as K , a relationship that follows from the fact that in these response processes, a high K means greater friction and lower adjustment time. According to Simons (personal communication), the spin-up times for an Ekman suction model of a constant depth are given by the expression

$$K^{-1} = \frac{a}{H} \text{ s} \quad \text{where } H \text{ is the mean depth of the lake}$$

where α is the stress coefficient as discussed in section 2.1. However, I have chosen to use the Ekman depth instead of the mean depth of the lake because the region directly affected by vertical friction is of the order of the Ekman layer thickness (Pedlosky, 1979). The spin-up times given in Table 4.1 for the model are in reasonable agreement with those for an Ekman suction model of constant depth which are given in Table 4.2 below :

K (sec^{-1})	Spin-up time (K^{-1}) in hours
$0.01/D_E$	102
$0.025/D_E$	41
$0.05/D_E$	20

Table 4.2 : Spin-up times for an Ekman suction model of constant depth. D_E is the Ekman depth for Lake Melville of thirty-seven meters which has been used in computing the above times instead of the mean depth of eighty-six meters (see text above).

The Ekman depth is computed by modifying equation (9.13) in Pond and Pickard (1978) for a wind drag coefficient of $C_d=0.002$ (which has been used in equation (1.2)) and getting the form

$$D_E = \frac{(4.7) W}{(\sin |\phi|)^{1/2}}$$

where W is the wind speed of seven meters per second and ϕ is the latitude of Lake Melville of fifty-two degrees north. This equation gives an Ekman depth of thirty-seven meters. The plots of total energy against time for a wind forcing episode lasting ten days for the first two cases, and fifteen days for the third case are presented in Figure 4.7. Since most of the energy in the lake is in the form of kinetic energy, the plots of the kinetic energy closely resemble those of total energy and the kinetic energy is about a thousand times greater than the potential energy (see Figure 4.8). The 'dip' in the first

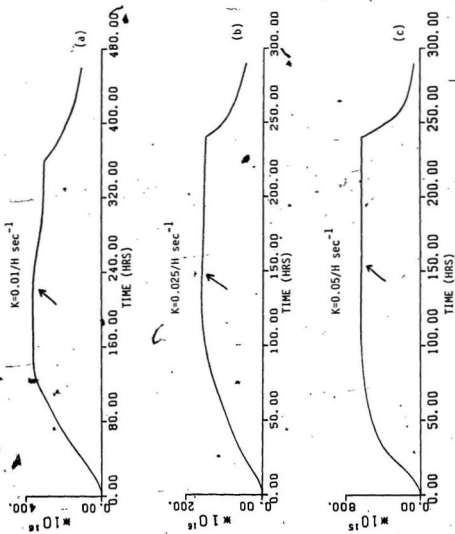


Figure 4.7 ; Total energy in Lake Melville (in ergs) for different values of bottom stress coefficient K as a function of time. The arrow in each plot indicates the beginning of a "dip" (see text).

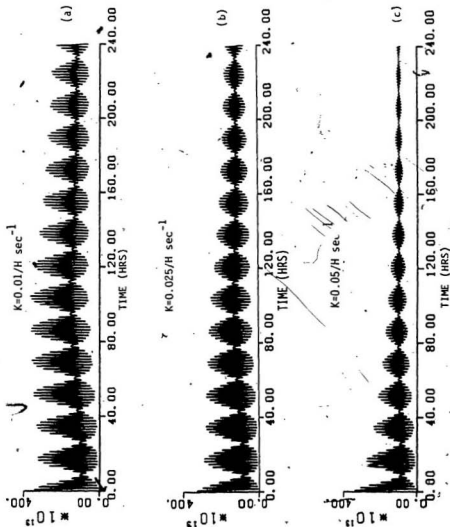


Figure 4.8 : Potential energy in Lake Melville (in ergs) as a function of time for different values of the bottom stress coefficient K_b during wind forcing only.

two plots may be due to some kind of a frictional adjustment or second order effects that are not clearly resolved.

The plots of potential energy against time for the same values of K are shown in Figure 4.8. There appear to be two types of oscillations present in these plots. The first type is due to the barotropic Kelvin wave and appears as the finer structure. The period is equal to the barotropic Kelvin wave period and can be explained as follows: Consider a motion of the form

$$\eta = A + B \sin \sigma_1 t + C \sin \sigma_2 t \quad (4.16)$$

where A , B and C are the largest surface elevation amplitudes due to the wind set-up, the Kelvin wave, and as will be shown, the near-inertial oscillations respectively. Let the external Kelvin wave and the inertial oscillations have frequencies of σ_1 and σ_2 . A Fourier transform analysis on Figure 4.8(b) indicates that the values of these frequencies correspond to periods of 1.6 and 17.5 hours respectively. From section 4.3, recall that potential energy is proportional to η^2 . If we square both sides of equation (4.16), we get the expression

$$\eta^2 = A^2 + 2AB \sin \sigma_1 t + 2AC \sin \sigma_2 t + 2BC \sin \sigma_1 t \sin \sigma_2 t + B^2 \sin^2 \sigma_1 t + C^2 \sin^2 \sigma_2 t. \quad (4.17)$$

The wind set-up is dominant at the surface, and its amplitude A is much greater than that due to the barotropic Kelvin wave or the inertial oscillations, estimated to be one centimeter. From the Fourier transforms, the uninodal Kelvin wave period is observed to be about 1.6 hours. This value is about the same as that computed to a first approximation from Merian's formula (equation (4.14)). From the contours in Figure 4.5, the estimated amplitude is about 0.5 centimeters. A second type of an oscillation which is a near-inertial one, which from the Fourier transform has a period of 17.5 hours, has an

amplitude of around 0.1 centimeters. The inertial period is usually given by

$$T_{\text{inertial}} = \frac{2\pi}{f} \quad (4.18)$$

which works out to be about 14.7 hours for Lake Melville. The 17.5 hour period is the inertial oscillation but probably has been shifted by frictional effects which depend on the water depth (see equation (2.20)).

When we put the frequencies and the amplitudes in this equation, we do not get the 'wave packets' that appear in Figure 4.8, however as will be shown later, this equation works for the two-layer model. The difficulty here would appear to be that the frictionally shifted inertial period depends on the local water depth and that the 17.5 hour period is therefore an average value. I feel that the use of this average period is not adequate to reproduce the wave packet structure of Figure 4.8 with equation (4.17).

CHAPTER 5 : THE TIME-DEPENDENT TWO-LAYER

MODEL OF LAKE MELVILLE

5.1. Introduction

In many fjords and estuaries, the density structure consists of two layers as is the case with Lake Melville. Such stratification gives rise to internal waves and other phenomenon of a baroclinic nature not found in homogeneous basins or barotropic systems. A two-layer model is therefore one step further up in complexity in the set of three models of Lake Melville considered here.

Although multilayer models are complicated to use in circulation studies because of various complications mentioned in section 5.1, data acquisition and analysis by Bobbit and Akenhead (1982), implies that the stratification of Lake Melville into an upper layer and a lower one is retained throughout the year (unlike the Great Lakes) and hence, homogeneous models of the lake are probably inadequate in representing the dynamics of the lake. The equations relevant to such a two-layer model are given by equations (2.22) to (2.27).

5.2. Total Circulation Energy for Two-Layer Basins

For a two-layer system, the total potential energy is given by

$$P.E. = \int_A \frac{\rho}{2} g(\eta^2 - \eta'^2) dA + \int_{A'} \frac{\rho}{2} g\eta'^2 dA' \quad (5.1)$$

where the first and the second integrals refer to the upper and the lower layers respectively.

The total kinetic energy in the lake is given by (Yuen, 1969)

$$\text{K.E.} = \int_V \frac{\rho}{2} (U^2 + V^2) dV + \int_V \frac{\rho'}{2} (U'^2 + V'^2) dV' \quad (5.2)$$

Again, the first and the second integrals refer to the upper and the lower layers respectively and are evaluated numerically. The total energy in this two-layer system is merely the sum of the total potential energy and the total kinetic energy.

5.3. The Surface and Internal Modes of a Two-Layer System

According to Proudman (1953), the solutions of the equations (2.22) to (2.27) are characterized by a number of wave-like modes or propagating disturbances of the surface and the interfacial elevations η and η' respectively. Given the coupling terms like η and η' in the equations of a two-layer system, these modes are not independent. The physical interpretation and mathematical formulations are greatly facilitated if a linear combination is made of the two sets of equations in section 2.2. Such a combination was considered by Veronis (1956) and resulted in the transformation of the equations of a two-layer system into an equivalent one-layer set as follows: suppose we use the linear combinations

$$U_1 = (1 - \beta_0)U + U' \quad (5.3)$$

$$V_1 = (1 - \beta_0)V + V'$$

$$\eta_1 = (1 - \beta_0)(\eta - \eta') + \eta'$$

$$F_i' = (1 - \beta_i)F + F'$$

where β_i ($i = 1, 2$) are the roots of Stoke's equation

$$\frac{h}{h'}\beta^2 - (1 - \frac{h}{h'})\beta + (1 - \frac{\rho}{\rho'}) = 0 \quad (5.4)$$

given by

$$\beta_i = \frac{h + h'}{2h} (1 \pm \sqrt{(1 - \frac{4hh'\epsilon}{(h + h')^2})}) \quad (5.5)$$

Let U and V denote the x and y components of volume transport rather than the depth averaged velocities for this section only. Equations (2.22) to (2.27) may be transformed into the three equations

$$\frac{\partial U_1}{\partial t} - fV_1 = -gh_1 \frac{\partial \eta_1}{\partial x} + F_1^{(x)} \quad (5.6)$$

$$\frac{\partial V_1}{\partial t} + fU_1 = -gh_1 \frac{\partial \eta_1}{\partial y} + F_1^{(y)} \quad (5.7)$$

$$\frac{\partial \eta_1}{\partial t} = -\frac{\partial U_1}{\partial x} - \frac{\partial V_1}{\partial y} \quad (5.8)$$

where the horizontal stresses F_i (Csanady (1968), notation) may be set to zero so that the free modes can be looked at more easily.

Consider the non-dimensional ratio

$$\epsilon = \frac{\rho' - \rho}{\rho} = 1 - \frac{\rho}{\rho'} \quad (5.9)$$

Since the quantity ϵ is always small in practice (of the order of 10^{-3}), the square root in

equation (5.12) can be expanded in Taylor Series. This enables us to write the roots β_i

$$\beta_1 = \frac{h' \epsilon}{h + h'} + O(\epsilon^2) \quad (5.10)$$

$$\beta_2 = 1 + \frac{h'}{h} - \frac{h'}{h} \epsilon + O(\epsilon^2)$$

If we let the depth h in the depth averaged equations of volume transport (5.13) to (5.15) be replaced by

$$h_1 = \epsilon \frac{h'}{\beta_1} \quad (5.11)$$

so that the equivalent depths are

$$h_1 = h + h' + O(\epsilon) \quad (5.12)$$

$$h_2 = \frac{\epsilon h h'}{h + h'} + O(\epsilon^2)$$

It now follows that the displacements η_i ($i=1,2$) become

$$\eta_1 = \eta - \frac{(\eta - \eta') h' \epsilon}{h + h'} + O(\epsilon^2) \quad (5.13)$$

$$\eta_2 = -\frac{h'}{h} \eta + \left(1 + \frac{h'}{h}\right) \eta' + \frac{(\eta - \eta') h' \epsilon}{h + h'} + O(\epsilon^2) \quad (5.14)$$

η_1 and η_2 in equations (5.13) and (5.14) are determined by the nature of the lake. A class of 'pure' modes results if $\eta_2 = 0$ and $\eta_1 \neq 0$ and from equation (5.14), it follows that

$$\frac{\eta}{\eta'} = 1 + \frac{b}{b'} + O(\epsilon) \quad (5.15)$$

the solutions for which include waves propagating with the phase velocity

$$C_1 = \sqrt{g b_1} \quad (5.16)$$

given for these modes by

$$C_1^2 = g(b + b') + O(\epsilon) \quad (5.17)$$

where b and b' are assumed to be independent of position and the wave is propagating along a straight wall. From equation (5.17), it is immediately clear that these modes are virtually indistinguishable from those found in homogeneous basins. These are the 'barotropic' modes which include the longitudinal and the rotating barotropic Kelvin waves as well as the inertial oscillations. These modes are also characterized by a maximum displacement at the surface.

If now we have the situation where $\eta_1 = 0$ and $\eta_2 \neq 0$, we get a second class of modes characterized by

$$\frac{\eta}{\eta'} = -\frac{\epsilon h'}{h + h'} + O(\epsilon^2) \quad (5.18)$$

$$C_2 = \sqrt{\frac{\epsilon g h h'}{h + h'}} + O(\epsilon^2) \quad (5.19)$$

which apply strictly to a stratified system (where h and h' are assumed to be constant for simplicity) since if ϵ tends to zero, these modes vanish as well. Here, the maximum displacements occur at the interface between the two layers. The wave propagation velocity C_2 as given by equation (5.19) is considerably smaller than that associated

with the surface modes. These are the baroclinic modes for a two-layer system and include the internal Kelvin waves and the Poincare waves.

For $i=1$ and $i=2$, the set of equations (2.22) to (2.27) yields two sets of solutions. The two-layer solution may be obtained by the inverse transformations

$$\eta' = \frac{b' \eta_1 + b \eta_2}{b + b'} \quad (5.20a)$$

$$\eta = \eta_1 - \left(1 - \frac{\rho}{\rho'}\right) \frac{\eta_2 b b'}{(b + b')^2} \quad (5.20b)$$

$$U^* = (U_1 - U_2) \frac{b}{b + b'} \quad (5.20c)$$

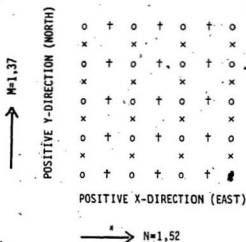
$$U' = \frac{b' U_1 - b U_2}{b + b'} \quad (5.20d)$$

The solutions for the y-components can be written similarly.

5.4. Method of Solution

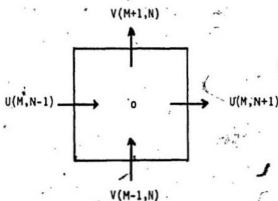
5.4.1 The Numerical System

Using the finite-difference expressions of the first order derivatives given in section 2.3, the equations of motion for the two-layer system given by equations (2.22) to (2.27) are transformed by finite differences into forms suitable for numerical solutions by the process of iteration. The form of centered difference schemes is suitable for a grid system like the Richardson lattice (Platzman, 1963) where the continuity equations may be evaluated at even time steps $2n\Delta t$, where $n=0,1,2,3,\dots$. Let t represent some even multiple of the time step Δt . In this grid (Figure 5.1) the mesh size in the x and the y directions is the same, i.e.,



o = η points
 + = u points
 x = v points

(a) Staggered grid



(b) Grid square

$H(M,N)$, $\eta(M,N)$, $U(M,N)$ and $V(M,N)$ defined at point o in grid square above.

Figure 5.1 : (a) the staggered grid representation of variables ; (b) the grid square.

$$\Delta x = \Delta y = \delta = 1.833 \text{ kilometers}$$

and all grid points that represent similar variables are displaced two grid spaces apart. The relative positions of the variables are as shown in Figure 5.1 and the variables are evaluated at the following points (Yuen, 1969)

$$\eta \text{ values at } M = \text{even}, N = \text{even and } T = \text{even} \quad (5.21)$$

$$U \text{ values at } M = \text{even}, N = \text{odd and } T = \text{odd}$$

$$V \text{ values at } M = \text{odd}, N = \text{even and } T = \text{odd}.$$

Although other types of grids may be used, for example one where all the variables are computed at each grid point (as used by Jelesnianski, 1964), this particular grid was chosen over the Jelesnianski-type grid because the gradient approximations have errors proportional to δ^2 which are of a lower order than the errors proportional to $(2\delta)^2$ for the grid used by Jelesnianski.

In representing the variables in accordance with (5.28), M , N and T will denote the even space and time indices, and $M \pm 1$, $N \pm 1$ and $T \pm 1$ the odd space and time indices.

The boundary and the initial conditions are the same as those used for the time-dependent homogeneous model (see section 4.4.2) and are applied separately to each layer in this two-layer model.

5.4.2. Continuity Equations

The equations of continuity (2.24) and (2.27) are evaluated before the other equations in the solution technique used here. This requires that all variables be zero at some initial time.

Let t represent some even multiple of the time step Δt . Consider equation (2.27) in its finite difference form

$$\left(\frac{\partial \eta'}{\partial t}\right)^i + \Delta t = - \left(\frac{\partial h' U'}{\partial x}\right)^i + \Delta t - \left(\frac{\partial h' V'}{\partial y}\right)^i + \Delta t \quad (5.22)$$

Now if $(\eta')^i$ is known from the previous time step, then the rearrangement of a central difference expression for $\left(\frac{\partial \eta'}{\partial t}\right)^i + \Delta t$ gives

$$(\eta')^i + \Delta t = 2\Delta t \left(\frac{\partial \eta'}{\partial t}\right)^i + \Delta t + (\eta')^i \quad (5.23)$$

Similarly, the remaining continuity equation (2.24) may be evaluated if η^i is known from a previous time step. Using the relation

$$(\eta)^i + \Delta t = 2\Delta t \left(\frac{\partial \eta}{\partial t}\right)^i + \Delta t + (\eta)^i \quad (5.24)$$

along with the expression (5.25), the equation (5.3) is finally evaluated in accordance with

$$\left(\frac{\partial (\eta - \eta')}{\partial t}\right)^i + \Delta t = - \left(\frac{\partial (hU)}{\partial x}\right)^i + \Delta t - \left(\frac{\partial (hV)}{\partial y}\right)^i + \Delta t \quad (5.25)$$

5.4.3. Momentum Equations

The dynamic equations (2.22) and (2.23) can be written as

$$\left(\frac{\partial U}{\partial t}\right)^t = (rV)^t - g\left(\frac{\partial \eta}{\partial x}\right)^t + (F_s^{(u)})^t - (F_i^{(u)})^t \quad (5.26)$$

$$\left(\frac{\partial V}{\partial t}\right)^t = -(rU)^t - g\left(\frac{\partial \eta}{\partial y}\right)^t + (F_s^{(v)})^t - (F_i^{(v)})^t \quad (5.27)$$

where t stands for an even multiple of the time step Δt . The stresses (F_s^t) and (F_i^t) are given by

$$(F_s^t) = \left(\frac{\tau}{h\rho}\right)^t \quad (5.28)$$

$$(F_i^t) = \frac{C_i}{h'\rho'} (\bar{U} - \bar{U}')^t \quad (5.29)$$

$$(F_b^t) = \frac{C_b}{h'\rho'} (\bar{U}')^t \quad (5.30)$$

In equations (5.28) to (5.30), the interfacial and bottom stress coefficients C_i and C_b are defined by equations (2.28) and (2.29) respectively. Now, rearranging central difference schemes in time as

$$(U)^{t+\Delta t} = 2\Delta t\left(\frac{\partial U}{\partial t}\right)^t + (U)^{t-\Delta t} \quad (5.31)$$

$$(V)^{t+\Delta t} = 2\Delta t\left(\frac{\partial V}{\partial t}\right)^t + (V)^{t-\Delta t} \quad (5.32)$$

and simply time-stepping with $U^{t-\Delta t}$ known from the previous time step, equation

(5.20) is evaluated if $V^{i+\Delta t}$ and $\eta^{i+2\Delta t}$ are known. $V^{i+\Delta t}$ is obtained by an expression similar to (5.23) and $\eta^{i+2\Delta t}$ is known from the results of section (5.25) at even time steps. Similarly, the dynamical equations (2.25) and (2.26) may be written as

$$\left(\frac{\partial U'}{\partial t}\right)^i = (rV')^i - \xi \frac{\rho}{\rho'} \left(\frac{\partial \eta}{\partial x}\right)^i - \xi \left(1 - \frac{\rho}{\rho'}\right) \left(\frac{\partial \eta'}{\partial x}\right)^i + (F_1^{(u)})^i - (F_0^{(u)})^i \quad (5.33)$$

$$\left(\frac{\partial V'}{\partial t}\right)^i = -(rU')^i - \xi \frac{\rho}{\rho'} \left(\frac{\partial \eta}{\partial y}\right)^i - \xi \left(1 - \frac{\rho}{\rho'}\right) \left(\frac{\partial \eta'}{\partial y}\right)^i + (F_1^{(v)})^i - (F_0^{(v)})^i \quad (5.34)$$

where ξ is defined as for equations (5.20) and (5.27). The time stepping is given by the schemes

$$(U')^{i+\Delta t} = 2\Delta t \left(\frac{\partial U'}{\partial t}\right)^i + (U')^{i-\Delta t} \quad (5.35)$$

$$(V')^{i+\Delta t} = 2\Delta t \left(\frac{\partial V'}{\partial t}\right)^i + (V')^{i-\Delta t} \quad (5.36)$$

along with the surface and interface elevation values as discussed in section 5.3.2.

5.4.4. Summary of the Computer Algorithm

In accordance with definitions (5.9), all spatial derivatives were evaluated using central difference schemes. Using the notation

$$F(M,N,T) = F[y=(M-1)\Delta y, x=(N-1)\Delta x, t=T\Delta t] \quad (5.37)$$

the hydrodynamical equations were put into finite difference forms. Here, the -1 terms were introduced to ease translation into FORTRAN IV as required by the computer algorithm of Yuen (1969).

In order to put equation (5.12) into its appropriate finite difference form, the

expression for $(\frac{\partial \eta}{\partial x})_{M,N+1,T}$ was written as

$$(\frac{\partial \eta}{\partial x})_{M,N+1,T} = \frac{1}{2\Delta x} [\eta(M,N+2,T) - \eta(M,N,T)] \quad (5.38)$$

The first term on the right hand side of equation (5.17) was written as

$$\begin{aligned} (\frac{\partial(h' U')}{\partial x})_{M,N,T+1} = & \frac{1}{2\Delta x} (h' (M,N+1,T+1) U' (M,N+1,T+1) \\ & - h' (M,N-1,T+1) U' (M,N-1,T+1)) \end{aligned} \quad (5.39)$$

and the second term as

$$\begin{aligned} (\frac{\partial(h' V')}{\partial x})_{M+1,N,T+1} = & \frac{1}{2\Delta x} (h' (M-1,N,T+1) U' (M-1,N,T+1)) \\ & - (h' (M+1,N,T+1) V' (M+1,N,T+1)) \end{aligned} \quad (5.40)$$

where h' has been corrected for depth using the expression

$$h' (M,N\pm 1,T+1) = D(M,N\pm 1) + \eta' (M,N\pm 1,T\pm 1) \quad (5.41)$$

Here, $D(M,N)$ is the thickness of the bottom layer initially at time $t=0$. But η' is not known at odd times $T\pm 1$. Therefore, we use the finite difference scheme to define $(\eta')_{M,N,T+1}$ as required by (5.21) as

$$(\frac{\partial \eta'}{\partial t})_{M,N,T+1} = \frac{1}{2\Delta t} (\eta' (M,N,T+1) - \eta' (M,N,T)) \quad (5.42)$$

which gives the value of η' at time step $T+2$ assuming that the value at the previous time step T is known. Equation (5.35) is then evaluated for η since η' is known beforehand in this order.

Equations (5.26) and (5.27) have to be evaluated in accordance with convention (5.35). Though U and V are both evaluated at odd time steps by using equations (5.31) and (5.32) in addition to equations (5.26) and (5.27), U and V are evaluated at points adjacent to each other on the grid. We use the equations (from simple interpolation)

$$U(M+1,N,T) = \frac{1}{4} [U(M,N+1,T-1) + U(M+2,N+1,T-1) + U(M,N-1,T-1) + U(M+2,N-1,T-1)] \quad (5.43)$$

and

$$V(M,N+1,T) = \frac{1}{4} [V(M+1,N,T-1) + V(M+1,N+2,T-1) + V(M-1,N,T-1) + V(M-1,N+2,T-1)] \quad (5.44)$$

For equations (5.33) and (5.34), similar arguments allow the finite difference forms to be written in accordance with the convention (5.21).

The derivatives are evaluated using central differences as

$$\left(\frac{\partial U}{\partial t} \right)_{M,N+1,T} = \frac{1}{2\Delta t} [U(M,N+1,T+1) - U(M,N+1,T-1)] \quad (5.45)$$

and

$$\left(\frac{\partial V}{\partial t} \right)_{M+1,N,T} = \frac{1}{2\Delta t} [V(M+1,N,T+1) - V(M+1,N,T-1)] \quad (5.46)$$

for the velocities in the upper and lower layers. The gradient term for both the surface and interfacial elevations is written as

$$\left(\frac{\partial \eta}{\partial x} \right)_{M,N+1,T} = \frac{1}{2\Delta x} [\eta(M,N+2,T) - \eta(M,N,T)] \quad (5.47)$$

and

$$\left(\frac{\partial \eta}{\partial y}\right)_{M+1,N,T} = -\frac{1}{2\Delta y} [\eta(M+2,N,T) - \eta(M,N,T)] \quad (5.48)$$

Using these finite difference forms in equations (2.22) to (2.27) the equations in their final, iterable form are

$$\eta'(M,N,T+2) = \eta'(M,N,T) \quad (5.49)$$

$$\begin{aligned} & - \frac{\Delta t}{\Delta x} [b'(M,N+1,t) U'(M,N+1,T) \\ & - b'(M,N-1,T) U'(M,N-1,T) \\ & + b'(M+1,N,T) V'(M+1,N,T) \\ & - b'(M-1,N,T) V'(M-1,N,T)] \end{aligned}$$

$$\eta(M,N,T+2) = \eta(M,N,T) + \eta'(M,N,T+2) - \eta'(M,N,T) \quad (5.50)$$

$$\begin{aligned} & - \frac{\Delta t}{\Delta x} [b(M,N+1,T) U(M,N+1,T) \\ & - b(M,N-1,T) U(M,N-1,T) \\ & + b(M+1,N,T) V(M+1,N,T) \\ & - b(M-1,N,T) V(M-1,N,T)] \end{aligned}$$

$$U(M,N+1,T+1) = U(M,N+1,T-1) \quad (5.51)$$

$$\begin{aligned} & + \left(\frac{\Delta t}{2}\right) [V(M+1,N,T-1) + V(M+1,N+2,T-1) \\ & + V(M-1,N,T-1) + V(M-1,N+2,T-1)] \\ & - \frac{\Delta t}{\Delta x} [\eta(M,N+2,T) - \eta(M,N,T)] \\ & + 2\Delta t F_1^{(1)}(M,N+1,T) - 2\Delta t F_1^{(2)}(M,N+1,T) \end{aligned}$$

$$\begin{aligned}
 V(M+1, N, T+1) = & V(M+1, N, T-1) \\
 & + r \frac{\Delta t}{2} [U(M+2, N+1, T) + U(M+2, N-1, T-1) \\
 & + U(M, N+1, T-1) + U(M, N-1, T-1)] \\
 & - g \frac{\Delta t}{\Delta x} [\eta(M+2, N, T) - \eta(M, N, T)] \\
 & + 2\Delta t F_b^{(v)}(M+1, N, T) - 2\Delta t F_b^{(v)}(M+1, N, T)
 \end{aligned} \tag{5.52}$$

$$\begin{aligned}
 U'(M, N+1, T+1) = & U'(M, N+1, T-1) \\
 & + r \frac{\Delta t}{2} [V'(M+1, N, T-1) + V'(M+1, N+2, T-1) \\
 & + V'(M-1, N, T-1) + V'(M-1, N+2, T-1)] \\
 & - g \frac{\rho}{\rho'} \frac{\Delta t}{\Delta x} [\eta(M, N-2, T) - \eta(M, N, T)] \\
 & - g(1 - \frac{\rho}{\rho'}) \frac{\Delta t}{\Delta x} [\eta'(M, N+2, T) - \eta'(M, N, T)] \\
 & + 2F_b^{(u)}(M, N+1, T) - 2F_b^{(u)}(M, N+1, T)
 \end{aligned} \tag{5.53}$$

$$\begin{aligned}
 V'(M+1, N, T+1) = & V'(M+1, N, T-1) \\
 & + r \frac{\Delta t}{2} [U'(M, N+1, T-1) + U'(M+2, N+1, T-1) \\
 & + U'(M, N-1, T-1) + U'(M+2, N-1, T-1)] \\
 & - g \frac{\rho}{\rho'} \frac{\Delta t}{\Delta x} [\eta(M-2, N, T) - \eta(M, N, T)] \\
 & - g(1 - \frac{\rho}{\rho'}) \frac{\Delta t}{\Delta x} [\eta'(M+2, N, T) - \eta'(M, N, T)] \\
 & + 2\Delta t F_b^{(v)}(M+1, N, T) - 2\Delta t F_b^{(v)}(M+1, N, T)
 \end{aligned} \tag{5.54}$$

where

$$F_d(M, N, T) = \frac{C_1}{b\rho} [\bar{U}(M, N, T) - \bar{U}'(M, N, T)]$$

$$F_d(M, N, T) = \frac{C_b}{\rho(b+b')} [\bar{U}'(M, N, T)]$$

$$\bar{P}_s(M,N,T) = \frac{\bar{T}_s}{h_R}$$

5.5. Results of the Model

5.5.1. The Velocity Field in the Basin

For all the simulations of this model, a constant wind impulse lasting for one day was used. The velocity field in the upper layer is shown in Figure 5.2 for the value $\epsilon = 0.013$. Initially, the acceleration is in the direction of the wind in the early stages of wind forcing (not shown here) though in the later stages of the simulation, the velocity field is affected by the baroclinic effects in the system.

Plots of the x component of the velocity field at selected points are presented in Figure 5.3. It can be seen from these plots that there are two types of oscillations present. The large peaks are due to the internal Kelvin wave oscillation (the rotating internal Kelvin wave) the period of which is given by (Csanady, 1982)

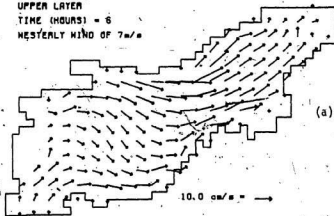
$$T_{\text{internal}} = \frac{L}{\sqrt{g \frac{\Delta \rho}{\rho} \frac{h h'}{h + h'}}} \quad (5.55)$$

where L is the perimeter of the lake which is about 340 kilometers and h and h' are the average thicknesses of the upper and lower layers equal to fifteen and seventy-one meters respectively. It is possible to take the thicknesses as such because the internal radius of deformation given by

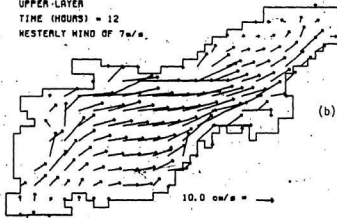
$$R_{\text{internal}} = \frac{\sqrt{g \frac{\Delta \rho}{\rho} \frac{h h'}{h + h'}}}{f} \quad (5.56)$$

Figure 5.2 ; Velocity field in the upper layer at various stages in the simulation. The wind cut-off is at twenty-four hours after onset.

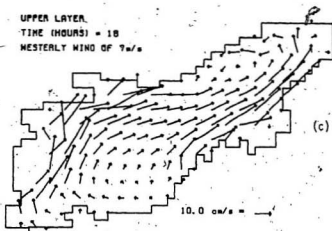
UPPER LAYER
TIME (HOURS) = 6
WESTERLY WIND OF 7m/s



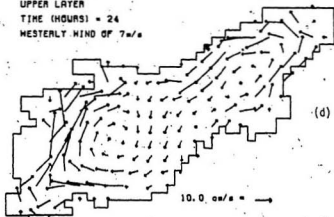
UPPER LAYER
TIME (HOURS) = 12
WESTERLY WIND OF 7m/s



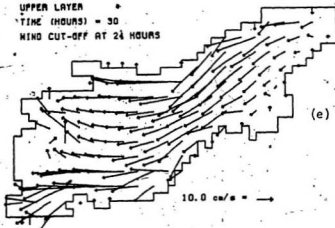
UPPER LAYER
TIME (HOURS) = 18
WESTERLY WIND OF 7 m/s



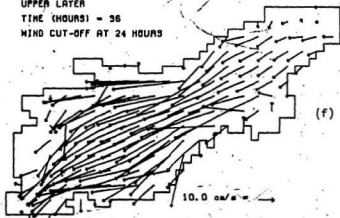
UPPER LAYER
TIME (HOURS) = 24
WESTERLY WIND OF 7 m/s



UPPER LAYER
TIME (HOURS) = 30
WIND CUT-OFF AT 24 HOURS



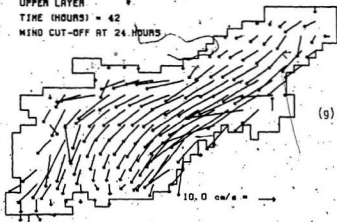
UPPER LAYER
TIME (HOURS) = 36
WIND CUT-OFF AT 24 HOURS



UPPER LAYER

TIME (HOURS) = 42

WIND CUT-OFF AT 24 HOURS



UPPER LAYER

TIME (HOURS) = 48

WIND CUT-OFF AT 24 HOURS

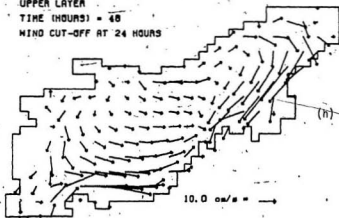
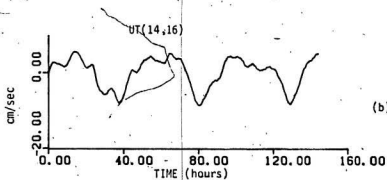
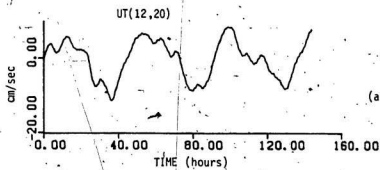
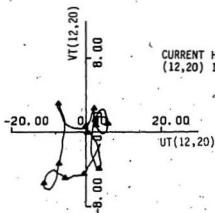


Figure 5.3 ; (a) x-component of velocity, at point (12,20) in the upper layer as a function of time ; (b) x-component of velocity at point (14,16) in the upper layer as a function of time ; (c) current hodograph at point (12,20); (d) current hodograph at point (14,16).

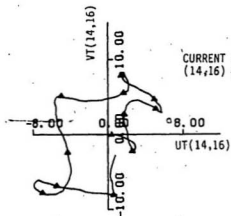
-90-





CURRENT HODOGRAPH FOR POINT
(12,20) IN THE UPPER LAYER.

(c)



CURRENT HODOGRAPH FOR POINT
(14,16) IN THE UPPER LAYER.

(d)

(each point on these curves represents
a time interval of four hours)

(where h and h' are the average thicknesses of the upper and the lower layers of fifteen and seventy-one meters respectively) is about eight kilometers and extends almost to the talweg of the lake. From the simulations, this internal Kelvin wave period is found to be about 55 to 60 hours and is in good agreement with a first order estimate of 60 hours obtained from equation (5.55) above. The smaller oscillations have a period of about 15 hours which is close to the theoretical inertial period of 14.7 hours computed from the formula

$$T_{\text{inertial}} = \frac{2\pi}{f} \quad (5.57)$$

and may be due to such oscillations.

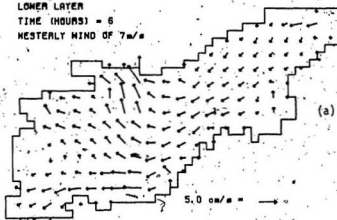
Current hodographs (Figures 5.3(c) and 5.3(d)) for the points (12,20) and (14,16) indicate that the current vectors at these points in the lake rotate in a counter-clockwise direction since the internal Kelvin wave oscillations (or the rotating internal Kelvin waves) are stronger than the inertial effects. However, the inertial effects are still apparent in these current hodographs since they tend to deflect the hodograph to the right at various points. This is typical behaviour for the currents towards the center of the lake and again suggests that the period of the largest oscillations may be of the order of about fifty to sixty hours. Along both the upper and the lower shores of the lake, a 'coastal jet' phenomenon (Csanady, 1968) occurs during the wind forcing episode (Figures 5.2(a) to 5.2(d)). The net current is in the direction of the wind and is part of the 'quasi-static' response of the lake. A response in the opposite direction develops after the wind cut-off.

The velocity field in the lower layer is shown in Figure 5.4. The currents here are only about half as large as those in the upper layer. It is clear from Figures 5.2 and 5.4 that the current directions in the upper and lower layers are directly opposite to each other in direction. As for the upper layer, the currents in the lower layer also appear to

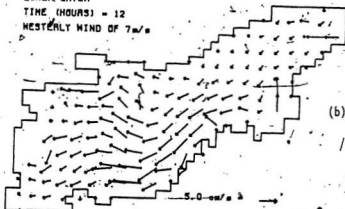
Figure 5.4 ; Velocity field in the lower layer at various stages in the simulation. The wind cut-off is at twenty-four hours after the onset.

2

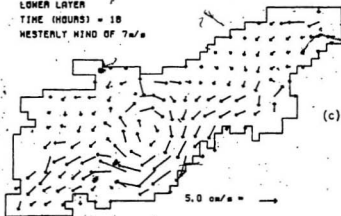
LOWER LAYER
TIME (HOURS) = 8
WESTERLY WIND OF 7 m/s



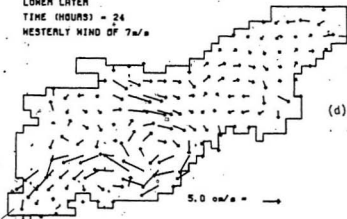
LOWER LAYER
TIME (HOURS) = 12
WESTERLY WIND OF 7 m/s



LOWER LAYER
TIME (HOURS) = 18
WESTERLY WIND OF 7 m/s



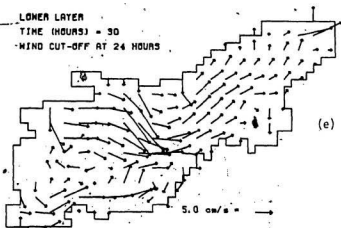
LOWER LAYER
TIME (HOURS) = 24
WESTERLY WIND OF 7 m/s



LOWER LAYER

TIME (HOURS) = 30

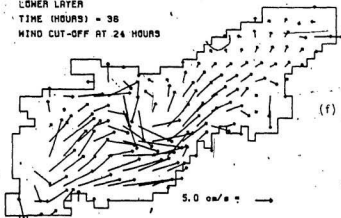
WIND CUT-OFF AT 24 HOURS



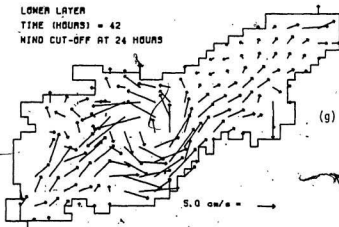
LOWER LAYER

TIME (HOURS) = 36

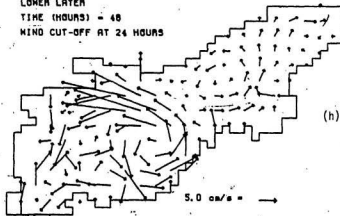
WIND CUT-OFF AT 24 HOURS



LOWER LAYER
TIME (HOURS) = 42
WIND CUT-OFF AT 24 HOURS



LOWER LAYER
TIME (HOURS) = 48
WIND CUT-OFF AT 24 HOURS



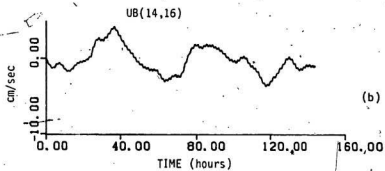
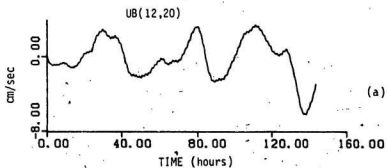
rotate cyclonically with a period similar to that of the rotating internal Kelvin wave. This is illustrated more vividly by plots of the x components of velocity and current hodographs at selected points in Figure 5.5. Unlike the velocity vectors in the upper layer, the ones for the bottom layer show the barotropic oscillations due to the longitudinal Kelvin wave as 'fine structure' in the curves. The fundamental barotropic Kelvin wave period of about 1.5 hours is apparent from Figure 5.5 and is in approximate agreement with that computed from the Merian formula (equation (4.20)) for $n=1$. Motions in Lake Melville away from the boundaries in the upper and the lower layers display an oscillatory character more strongly than the coastal zones which are dominated by a 'quasi-static' response. The fact that the internal radius of deformation as given by equation (5.56) is about eight kilometers means that coastally trapped waves do not influence the circulation pattern much beyond this distance. The motion away from the boundaries within this internal radius of deformation is therefore dominated by baroclinic effects due the internal Kelvin waves and inertial oscillations due to Poincare waves offshore. This also causes the pycnocline excursion to be the greatest near the boundaries and to decrease rapidly away from the shores (shown in Figures 5.6 and 5.7).

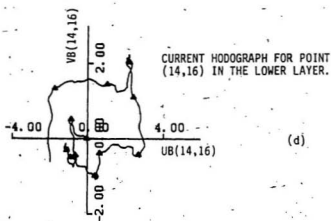
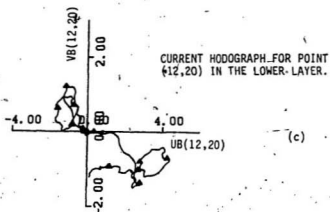
5.5.2. Response of the Surface and the Interface.

The contours of surface elevation of Lake Melville are shown in Figure 5.6 during and after the wind forcing episode. The numbers on the axes represent the distance scale multiplied by the grid mesh size of 1.833 kilometers.

As the westerly wind is applied to the lake, water starts to pile up at the eastern end of the basin with the opposite happening at the western end. Because of the effect of the Coriolis force, the water is deflected to the south until the surface slopes upwards to the southeast during the forcing episode. Figure 5.7 is a plot of the surface elevation as a function of time at two points located at the opposite ends of the basin. The oscillations appear to have a period of about 1.5 hours which is the barotropic Kelvin wave

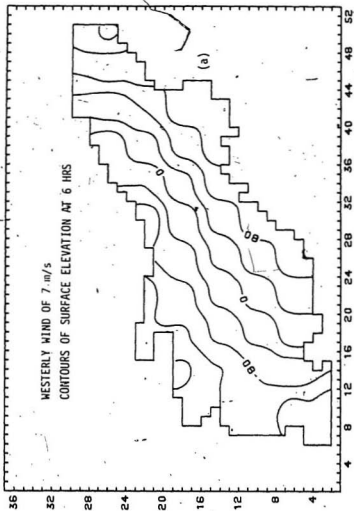
Figure 5.5 ; (a) x-component of velocity at point (12,20) in the lower layer as a function of time ; (b) x-component of velocity at point (14,16) in the lower layer as a function of time ; (c) current hodograph at point (12,20); (d) current hodograph at point (14,16).

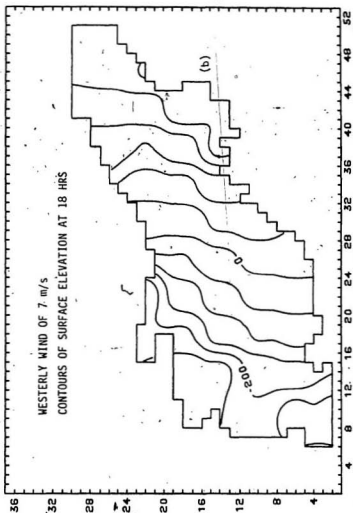


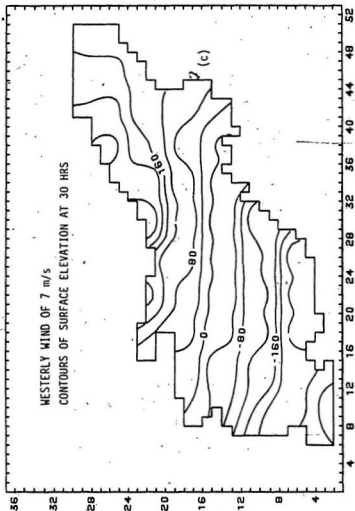


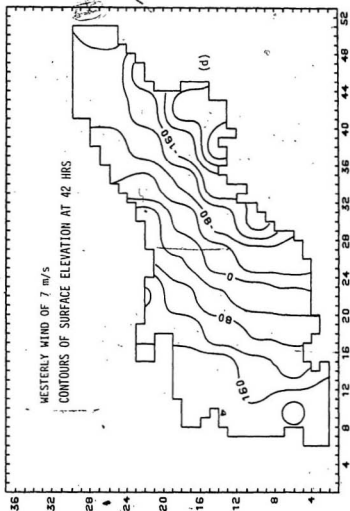
(each point on these curves represents
a time interval of four hours)

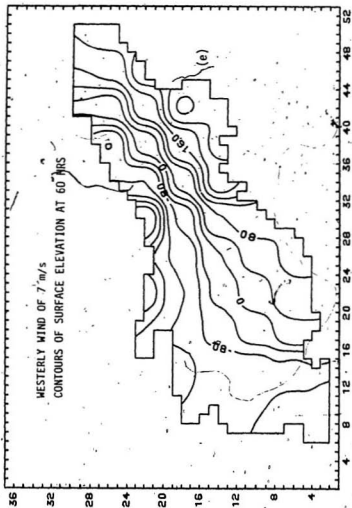
Figure 5.6 ; Contours of surface elevation in centimeters of Lake Melville at different stages in the simulation. Wind cut-off is at twenty-four hours from onset. (all values multiplied by a factor of 100)











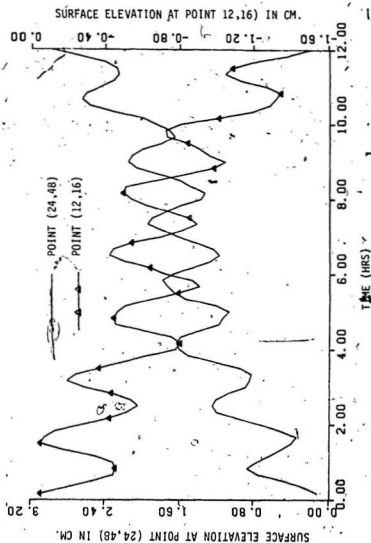


Figure 5.7 : Surface elevation at selected points at the opposite ends of the lake as a function of time during the first twelve hours of wind forcing.

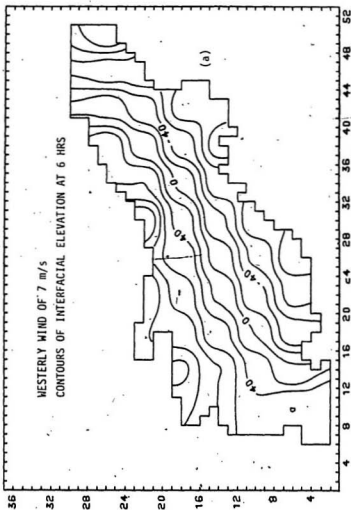
period where the interface displacement is roughly the same order of magnitude as the surface elevation as implied by equation (5.15). At all times, there appears to be a quasi-geostrophic balance in the cross shore direction, especially near the shores.

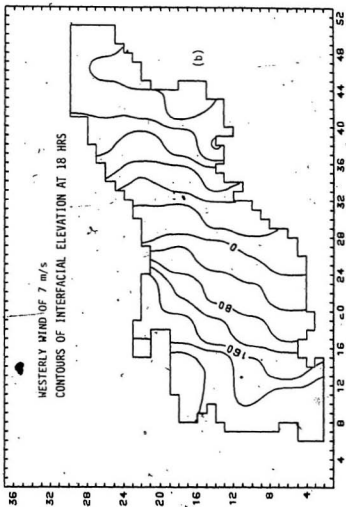
The greatest influence on the interface of the lake is due to the internal Kelvin waves, and the associated baroclinic effects at wind setup when the changes in the interfacial elevation are an amplified mirror image of the surface changes. This second class of modes is implied by equation (5.18). The interfacial behaviour is predominantly of a baroclinic nature being due to the presence of an internal rotating Kelvin wave which propagates cyclonically around the basin with a period of about 60 hours. The wavelength of this Kelvin wave is equal to the perimeter of the basin.

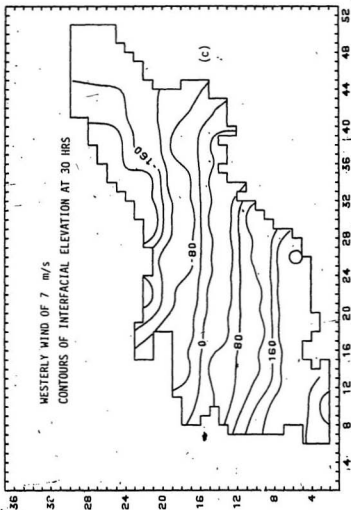
From Figure 5.8, the maximum downward displacement at the interface is found to the right of the wind. The maximum upward displacement is to the left of the wind. This is an internal Kelvin wave of a large amplitude which propagates cyclonically around the basin and is apparent from the motion of the 'zero' contour which moves around the basin (Figure 5.8). The longshore component of velocity is in geostrophic balance with the pressure gradient as can be seen from these figures and those of the velocity field in the upper and the lower layers (Figures 5.2 and 5.4). The high pressure is to the right of the current vectors in the nearshore zones so the 'light to right' rule is followed.

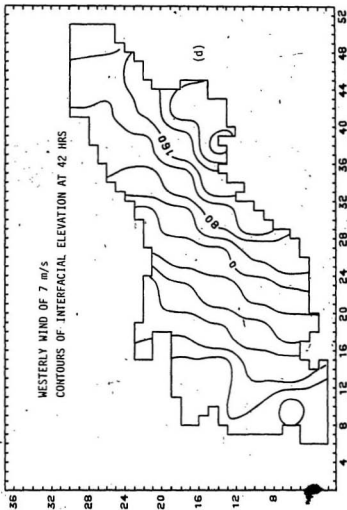
From Figure 5.8, one can get an idea of the speed of this internal Kelvin wave by following the 'zero contour'. It appears that the average speed of the wave is about 1.24 m/s at the shore. The period of this wave seems to be about fifty to sixty hours, since this is the amount of time it takes for the zero contour to complete one rotation. This is in agreement with first order calculations using equation (5.55). For Lake Melville, the phase speed of the internal Kelvin wave turns out to be about 1.27 m/s from the formula

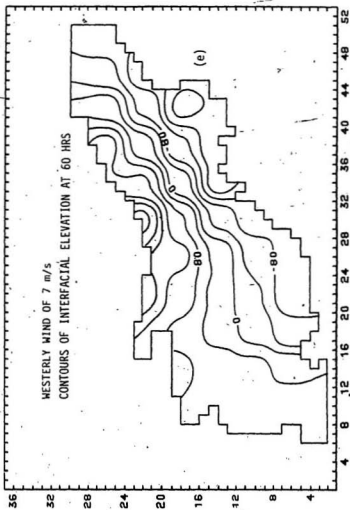
Figure 5.8 ; Contours of interfacial elevation of Lake Melville in centimeters at various stages in the simulation. Wind cut-off is at twenty-four hours from onset.











$$C_{\text{internal}} = \sqrt{g \frac{\Delta \rho}{\rho'} \frac{hb'}{h+b'}} \quad (5.58)$$

(where h and h' are the average thicknesses of the upper and lower layers of fifteen and seventy-one meters respectively) and is in very good agreement with the result from the model. The large scale vertical movements of the pycnocline near the shores that accompany these Kelvin waves lead to a very rapid generation of vorticity which affects the currents here. Since the rotating internal Kelvin wave is a coastally trapped wave, the motions associated with it are dominant in the nearshore regions.

The offshore regions of Lake Melville, and indeed most stratified lakes (Simons, 1980), are affected by the Poincare waves that have near-inertial frequencies and amplitudes which are much smaller than those of the internal Kelvin waves as the current vector plots (Figures 5.3 and 5.5) suggest. Figures 5.7 and 5.8 show that the highest values of both the surface and the interfacial elevation are in the nearshore regions.

5.8. Energy Distribution in Lake Melville

The plots of potential energy as a function of time are presented in Figure 5.9. There are two types of oscillations evident in the upper layer as Figure 5.9(a) shows. The finer structure of the curve represents the barotropic oscillations with a period closely resembling the fundamental Merian period of 1.5 hours. In this particular case, the potential energy oscillates at the period of the external (or barotropic) Kelvin wave (as for the homogeneous model).

A second type of oscillation is evident here in Figure 5.9(a). The period of this oscillation is twenty-five to thirty hours which is roughly one-half of the internal Kelvin wave period discussed earlier. This can be explained as follows: Suppose we have the surface elevation given by equation (4.16). Recall that potential energy is proportional to

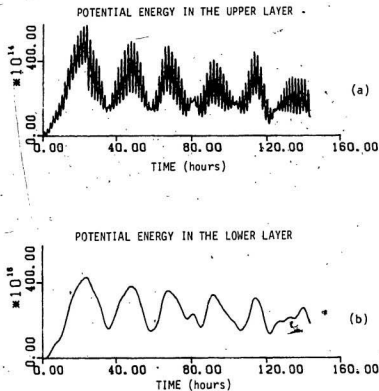


Figure 5.9 ; Potential energy in each layer of Lake Melville (in ergs) as a function of time.

the surface elevation squared as given by the expression (4.17), which upon the use of trigonometric identities becomes

$$\eta^2 = A^2 + 2 A B \sin \sigma_1 t + 2 A C \sin \sigma_2 t + 2 B C \sin \sigma_1 t \sin \sigma_2 t \\ + \frac{B^2}{2} - \frac{B^2}{2} \cos 2 \sigma_1 t + \frac{C^2}{2} - \frac{C^2}{2} \cos 2 \sigma_2 t.$$

Here, the frequencies σ_1 and σ_2 are due to the baroclinic effects at the interface (the internal Kelvin wave) and the inertial effects respectively. Since the surface elevation is a 'reflection' of the interfacial elevation (Yuen, 1969), the amplitude B which results from these baroclinic effects is dominant over the other amplitudes A and C which result from the wind setup and the inertial effects respectively. Consequently, the most dominant terms in this equation are those containing B^2 , in particular, the sixth and the seventh terms on the right hand side of the above equation. In these terms, the frequency appears at twice its initial value and hence the period is halved.

The potential energy as a function of time in the lower layer is plotted in Figure 5.9(b). Since the interfacial elevation is much greater than the surface elevation, it could be expected that the potential energy of the lower layer is correspondingly greater than that of the upper layer (in fact, greater by a factor of a 100) and the simulations bear this out. As for the upper layer, evidence of the internal Kelvin wave appears in the form of oscillations that have a period of twenty-five to thirty hours (as explained earlier). There is no evidence of a barotropic component here possibly because of the lack of sufficient resolution in the plot.

The kinetic energy as a function of time is presented in Figure 5.10 for each of the two layers. The profiles of kinetic energy are quite similar for both layers, and since the highest velocities are in the upper layer, the kinetic energy is about twice as high there as in the lower layer. From Figure 5.10(a), it is apparent that the baroclinic component again dominates the upper layer. Oscillations with a period of twenty-five to thirty

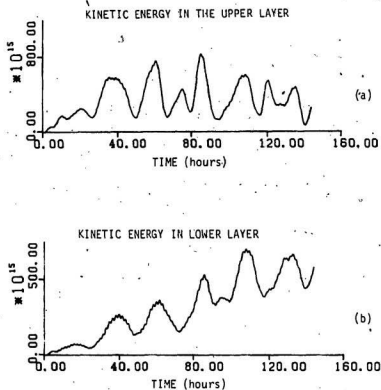


Figure 5.10 ; Kinetic energy in each layer of Lake Melville (in ergs) as a function of time.

hours are evident in the upper layer. The kinetic energy associated with the lower layer is shown in Figure 5.10(b). In addition to the thirty hour oscillations visible here, finer peaks due to the barotropic component are more pronounced here than in the upper layer though they have the same approximate period of about 1.5 hours. The kinetic energy here increases with time possibly because of a transformation from the potential energy which appears to decrease at the same time (Figure 5.9(b)). Such a transformation seems to be over a long time scale.

Figure 5.11 shows plots of the total potential and kinetic energies in the system, as well as the total overall energy in the system as a function of time. The oscillations due to the internal Kelvin wave dominate the total kinetic energy of the system. This is true as well for the total energy in the system. This indicates that the baroclinic component dominates the dynamics of a two-layer system while the inertial oscillations appear to be less significant in a lake such as this.

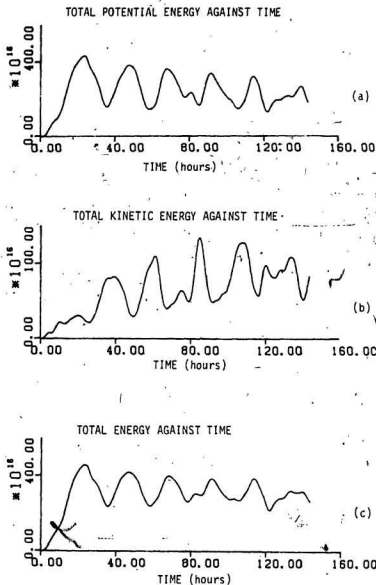


Figure 5.11; Total energy distribution in Lake Melville (in ergs) as a function of time.

CHAPTER 6 : DISCUSSION

6.1. Introduction

This chapter discusses the implications of the various models considered in this thesis. The strengths and weaknesses of each model are pointed out, and possible improvements suggested. Some simple field measurements are suggested since the lack of field data from the area means that the models cannot be calibrated, or that numerical results cannot be compared to observed data. Field data are needed to more effectively assess the validity of the models and to calibrate them.

6.2. General Discussion

The steady-state model of Lake Melville was considered because it was the easiest one to implement but still allowed the assessment of factors like wind directions and bottom stress coefficients. In view of the meteorological data available from the area, it was important to determine how the circulation pattern might be affected by the two most common winds in the area which happen to be the westerlies and the southwesterlies. As it turned out, the effect of using two different wind directions produced similar circulations and a westerly wind was chosen for all subsequent computations for this and other models. The steady-state model would probably be applicable when uniform or near-uniform westerly wind episodes of a duration of two days or longer occur. Such wind episodes are not uncommon for the Goose Bay area (personal communication with Mr. B. Boucestatlas, Goose Bay weather office). Since the spin-up time of the lake varies from one to three days for the range of the bottom stress values considered here, wind

episodes lasting for this length of time would give rise to 'quasi-steady' currents which may be reproduced by such a model. It was found that the effect of the bottom stress coefficient on the circulation pattern was not great, though the magnitude of the current was inversely proportional to it. It is obvious that field data are necessary before such a model can be calibrated and reproduce the quasi-steady circulation in Lake Melville. Since the greatest depth gradients occur in the nearshore zones which can lead to numerical instabilities, a greater resolution of these areas could be an improvement in the model.

The time-dependent homogeneous model of Lake Melville is the next step up in the degree of complexity of two-dimensional models. A time-dependent model brings into perspective the dynamics of a lake more clearly. In particular, the nature of the currents can be investigated during wind forcing which would be important if, as usual, the wind field is a function of time. If the wind field varies sufficiently such that the steady-state model no longer applies, then a time-dependent model should be used. An estimate of the corresponding response of the currents and the surface elevation can then be made again once calibration questions have been answered. This applies not only to models driven by wind, but in fact to those that are influenced by tidal forcing as well. Tidal forcing could be neatly studied in Lake Melville during the ice season since the ice insulates the water from the effects of the wind, and the only forcing is from the tides. As another point, one could also study the modification of tidal forcing by an ice cover. It should be realized that in general circulation features are mainly of interest in ice-free situations, and it would not be difficult to include tidal forcing by including a sinusoidal volume transport term. All the models considered here are linear which implies that the solutions due to the wind and tidal forcing are separable and the relative importance of each type can be evaluated more quantitatively. The results from this model are in good agreement with those from the steady-state homogeneous model as far as the circulation pattern is concerned (during wind forcing), further strengthening the argument that for

homogeneous basins the most important factor affecting circulation patterns is the bathymetry. As for the steady-state model, a possible improvement in the model would result probably from a better spatial resolution in the numerical grid, especially at the edge of the lake.

As discussed in chapter I of this thesis, Lake Melville is stratified throughout the year. The homogeneous time-dependent model discussed above does not consider the two-layer structure of the lake and the important question of frictional coupling between the two layers. The available data indicates that the two-layer approximation to the density profile is a very good one and hence the two-layer model is the most realistic one of all the models considered in this thesis.

This model of Lake Melville shows that the largest currents and hence most of the kinetic energy is in the upper layer. This is due to the strong stratification in the lake. As far as the bottom layer is concerned, the currents there are only about a half as strong as those in the upper layer. In view of this, it is important to concentrate any current measurements in future in the upper layer.

Since most of the effects in the two-layer model are of a baroclinic nature, it is important to realize that the Kelvin wave speed in such a two-layer model is affected very much by the depth at the shores (Simons, 1983) and it may be critical to select the layer thicknesses carefully to get coastal currents correct. For any subsequent investigations therefore, this factor would have to be looked at more thoroughly, especially when field data becomes available. In this two-layer model, most of the energy is in the form of potential energy (see Figure (5.11)(a)). In the time-dependent homogeneous model though, most of the energy is in the form of kinetic energy (Figures 4.7 and 4.8). Therefore, it is not possible to compare these models accurately with one another by using equations (5.3) and further investigation into this problem is beyond the scope of this work. At this time, the two-layer model cannot be forced for longer than three days

since the pycnocline grows in time to the point where it intersects the surface and shallow water theory becomes invalid. This is the most important limitation of this model which makes it difficult to study the response (i.e. the spin-up and spin-down) times of the lake. The thickness of the upper and lower layers at the shores in this model was set to fifteen and ten meters respectively in order to avoid this problem (suggested by Dr. Nelson Freeman). A possible improvement on the model will probably result from using wind episodes more characteristic of the area and retaining the non-linear terms in the equations of motion as well as resolving the nearshore zones more. An improvement on such a two-layer model would probably result from retaining non-linear terms in the equations of motion since it is quite probable that the neglect of these terms is not valid in the vicinity of the ends or 'corners' of the basin. The order of magnitude of the non-linear term (for the time-dependent homogeneous model) is $\frac{\partial u}{\partial x}$ for example, is about 10^{-4} cm/s² which is approximately the same as that of the wind stress term $\frac{T}{\rho H}$ near the eastern end of the lake. Since the ratio of these terms is about unity, the neglect of such non-linear terms is clearly invalid at the corners of the basin. Numerically, this model is complicated and time consuming. At this time, to the best of my knowledge, there are no other such models of lakes with which to compare the results of this two-layer model to.

6.3. Field Program

From the modelling effort here, it may be expected that any water level measurements should yield surface level fluctuations due to the Kelvin waves assuming that the contribution from the tidal oscillations can be filtered out. Since internal Kelvin waves are often difficult to observe in the field, the surface level variations in Lake Melville would probably be dominated by oscillations due to the barotropic Kelvin waves. Current observations in the upper layer, particularly offshore, will probably show fre-

quencies that are similar to those of the internal Kelvin wave oscillations. A 'coastal jet' may be detected near the shores, at least during any wind forcing episode as part of the quasi-static response of the lake. I propose using two current meters, water level recorders and thermistor chains at the points A and B (see Figure 3.1) located at the opposite ends of the lake. In accordance with the results of the two-layer model, I would expect to see oscillations due to both the external and the internal Kelvin waves. It is probable that the internal Kelvin wave will be observable as well in the surface variations which might be of about a one centimeter amplitude. According to the two-layer model, the currents are dominated by the internal Kelvin wave oscillations. There is also evidence of near-inertial oscillations of the Poincare wave which are relatively weak, so they may not be detectable in an actual field measurement. A thermistor chain could help in detecting the movements of the pycnocline at the points A and B. It may be possible to study tidal currents in Lake Melville by deploying current meter moorings through the ice period when wind forcing is not present. Even though the tidal effects have been neglected in this work, I expect that these will be easily observed in the field whether or not the ice is present. By far though, the most important parameter to be measured in the field would be the current at selected points in the lake because the coefficients of stress affect the current values directly in the simulations. Only after such field data become available would one be able to calibrate this two-layer model and determine the appropriate interfacial and bottom stress coefficients. Although the effects of other specifications of the interfacial and bottom stress on the current values have not been shown in this thesis, it is possible that in view of any future field data the linear lateral stress format used may not be adequate, and a quadratic or a quasi-linear specification (which have a very small effect the circulation pattern in the homogeneous models at least) may be required. However, until such a time as this data becomes available, it is very difficult to say what the best types of interfacial and bottom stress specifications are.

References

Bennett, J.R. (1974) ;

On the Dynamics of Wind-Driven Lake Currents. Journal of Physical Oceanography. 4, 400-414.

Bennett, J.R. (1978) ;

A Three-Dimensional Model of Lake Ontario's Summer Circulation. II. A Diagnostic Study. Journal of Physical Oceanography 8, 1095-1103.

Bhogal, A.S. (1984) ;

Wind Driven Circulation in Lake Melville. A paper presented at the 11th annual meeting of the Canadian Meteorological and Oceanographic Society, Dalhousie University, Halifax, Nova Scotia. June, 1984.

Bobbitt, J.; Akenhead, S. (1982) ;

Influence of Controlled Discharge from the Churchill River on the Oceanography of Groswater Bay, Labrador. Canadian Technical Report of Fisheries and Aquatic Sciences No. 1097. 41 pp.

Bonham-Carter, G., Thomas, J.H. (1973) ;

Numerical Calculation of Steady Wind-Driven Currents in Lake Ontario and the Rochester Embayment. Proc. 16th Conf. Great Lakes Research. International Assoc. Great Lakes Research. 640-662.

Csanady, G.T. (1967) ;

Large Scale Motion in Great Lakes. Journal of Geophysical Research.
72, 4151-4162.

Csanady, G.T. (1968) ;

Wind-Driven Summer Circulation in the Great Lakes. Journal of Geophysical Research. 73, 2579-2589.

Csanady, G.T. (1972) ;

Response of Large Stratified Lakes to Wind. Journal of Physical Oceanography. 2, 3-13.

Csanady, G.T. (1976) ;

Mean Circulation in Shallow Seas. Journal of Geophysical Research. 81,
5389-5399.

Csanady, G.T. (1982) ;

Circulation in the Coastal Ocean. D. Reidel Publishing Co., 279 pp.

Defant, A. (1961) ;

Physical Oceanography. Pergamon Press, v. 1, 700 pp.

Gedney, R.T. (1972) ;

Wind-Driven Currents in Lake Erie. Journal of Geophysical Research.
77, 2714-2723.

Gill, A.E. (1982) ;

Atmosphere-Ocean Dynamics. Academic Press. 662 pp.

Hadjitheodorou, C. (1967) ;

Wind Induced Circulation in a Shallow, Rectangular Basin. Ph. D Thesis, Cornell University.

Hansen, W. (1966) ;

Die Reproduktion der Bewegungsvorgänge im Meere mit Hilfe hydrodynamisch-numerischer Verfahren. Mitt. d. Inst. f. Meeresk. d. Univ. Hamburg V.

Harleman, D.R.F., Holley, Jr. E.R., Hoopes, J.A., Rumer,

Jr., R.R. (1962) ; The Feasibility of a Dynamic Model of Lake Michigan. Pub. No. 9, Great Lakes Res. Div., Inst. Sci. and Tech., University of Michigan.

Huang, J.C.K. (1977) ;

A General Circulation Model for Lakes. NOAA Technical Memorandum ERL GLERL-16.

Huang, J.C.K., Sloss, P.W. (1981) ;

Simulation and Verification of Lake Ontario's Mean State. Journal of Physical Oceanography. 11, 1548-1566.

Jeleznianski, C.P. (1965) ;

Numerical Calculation of Storm Tides Induced by a Tropical Storm Impinging on a Continental Shelf. Monthly Weather Review. 94, 379-394.

Kruger, H.B., Boucaud, A.A. (1963) ;

Meteorology of Goose Airport, Labrador. Canada-Department of

Transport-Meteorological Branch Technical Report 474.

Large, W.G., Pond, S. (1981) ;

Open Ocean Momentum Flux Measurements in Moderate to Strong Winds. Journal of Physical Oceanography. 11, 324-336.

Lee, K.W., Liggett, J.A. (1970) ;

Computation for Circulation in Stratified Lakes. ASCE Journal of the Hydraulics Division. 10, 2089-2113.

Liggett, J.A. (1969) ;

Unsteady Circulation in Shallow, Homogeneous Lakes. ASCE Journal of the Hydraulics Division. 4, 1273-1288.

Liggett, J.A., Hadjitheodorou, C. (1969) ;

Circulation in Shallow Homogeneous Lakes. ASCE Journal of Hydraulics Division. 2, 609-620.

Liggett, J.A., Lee, K.K. (1971) ;

Properties of Circulation in Stratified Lakes. ASCE Journal of the Hydraulics Division. 1, 15-29.

Miyazaki, M. (1965) ;

Numerical Computation of the Storm Surge of Hurricane Carla, 1961, in the Gulf of Mexico. Oceanographical Magazine. 17, 109-140.

Mortimer, C.H. (1952) ;

Water Movements in Lakes During Summer Stratification ; Evidence from the Distribution of Temperature in Windermere. Philosophical

Transactions of the Royal Society of London. 236, 355-403.

Munk, W.H. (1947) ;

A Critical Wind Speed for Air-Sea Boundary Process. Journal of Marine Research. 6, 203-218.

Murty, T.S., Rao, D.B. (1970) ;

Wind-Generated Circulations in Lakes Erie, Huron, Michigan and Superior. Proc. 13th Conf. Great Lakes Research. IAGLR. 927-941.

Palmen, E., Laurila, E. (1938) ;

Über die Einwirkung eines Sturmes auf den Hydrographischen Zustand in Nordlichen Ostseegebiet. Comment. phys-math., Helsingf., 10. 53 pp.

Pedlosky, J. (1979) ;

Geophysical Fluid Dynamics. Springer-Verlag. 624 pp.

Platzman, G.W. (1958) ;

Lattice Structure of the Finite-Difference Primitive and Vorticity Equations. Monthly Weather Review. 6, 285-292.

Pond, S., Pickard, G.L. (1978) ;

Introductory Dynamic Oceanography. Pergamon Press. 241 pp.

Proudman, J. (1953) ;

Dynamical Oceanography. Methuen, London. Wiley, New York. 409 pp.

Ramming, H.G., Kowalik, Z. (1980) ;

Numerical Modelling of Marine Hydrodynamics - Applications to

Dynamic Physical Processes. Elsevier Scientific Publishing Company.
368 pp.

Rao, D.B., Murty, T.S. (1970) ;

Calculation of the Steady State Wind-Driven Circulations in Lake Ontario. Arch. Met. Geoph. Biokl. 195-210.

Rossby, C.G., (1936) ;

On the Frictional Force Between Air and Water and on the Occurrence of a Laminar Boundary Layer Next to the Surface of the Sea. Papers in Physical Oceanography and Meteorology. 4, 20 pp.

Sheng, Y.P., Lick, W. (1978) ;

Numerical Computation of Three-Dimensional Circulation in Lake Erie : A Comparison of a Free-Surface Model and a Rigid Lid Model. Journal of Physical Oceanography. 8, 713-727.

Simons, T.J. (1974) ;

Verification of Numerical Models of Lake Ontario : Part I. Circulation in Spring and Early Summer. Journal of Physical Oceanography. 4, 507-523.

Simons, T.J. (1980) ;

Circulation Models of Lakes and Inland Seas. Canadian Bulletin of Fisheries and Aquatic Sciences Bulletin 203. 146 pp.

Simons, T.J. (1982) ;

Documentation of a Two-Dimensional X-Y Model Package for Computing Lake Circulations and Pollutant Transports. Unpublished

Manuscript.

Simons, T.J. (1983) ;

Resonant Topographic Response of Nearshore Currents to Wind Forcing. Journal of Physical Oceanography. 13, 512-523.

Simons, T.J. (1983) ;

Nearshore Response of Stratified Models to Wind Forcing. Unpublished Manuscript.

Smith, G.D. (1965) ;

Numerical Solution of Partial Differential Equations. Oxford University Press. 179 pp.

Taylor, G.I. (1915) ;

Eddy Motion in the Atmosphere. Phil. Trans. Roy. Soc. A 215 : 1-26.

Von Schwind, J.J. (1980) ;

Geophysical Fluid Dynamics for Oceanographers. Prentice-Hall, Inc. 307 pp.

Wilson, B. (1960) ;

Note on the Surface Wind Stress over Water at Low and High Wind Speeds. Journal of Geophysical Research. 65, 3377-3382.

Welander, P. (1957) ;

Wind Action on a Shallow Sea. Some Generalizations of Ekman's Theory. Tellus. 9, 45-52.

Yuen, K.B. (1969) ;

A Numerical Study of Large-Scale Motions in a Two-Layer Rectangular
Basin. M. Sc. Thesis, University of Waterloo, 119 pp.



